Additive Manufacturing 36 (2020) 101593

Contents lists available at ScienceDirect

Additive Manufacturing

journal homepage: www.elsevier.com/locate/addma

Full Length Article

Non-destructive simulation of node defects in additively manufactured lattice structures

Bill Lozanovski [a,b,*], David Downing [a,b], Rance Tino [a,b,e], Anton du Plessis [f,g], Phuong Tran [c], John Jakeman [h], Darpan Shidid [a], Claus Emmelmann [i], Ma Qian [a], Peter Choong [b,d], Milan Brandt [a,b], Martin Leary [a,b]

[a] RMIT Centre for Additive Manufacture, RMIT University, Melbourne, Australia
[b] ARC Training Centre in Additive Biomanufacturing, Australia[1]
[c] Department of Civil & Infrastructure Engineering, RMIT University, Melbourne, VIC, 3001, Australia
[d] St. Vincent's Hospital, Department of Surgery, Melbourne, 3000, Australia
[e] Peter MacCallum Cancer Centre, Melbourne, 3000, Australia
[f] Research Group 3DInnovation, Stellenbosch University, Stellenbosch, 7602, South Africa
[g] Department of Mechanical Engineering, Nelson Mandela University, Port Elizabeth, 6001, South Africa
[h] Center for Computing Research, Sandia National Laboratories, Albuquerque, 87185-1320, United States
[i] Fraunhofer Research Institution for Additive Manufacturing Technologies IAPT, Hamburg, 21029, Germany

ARTICLE INFO

Keywords:
Selective laser melting (SLM)
Lattice structures
Certification
Computed tomography (CT)
Defects

ABSTRACT

Additive Manufacturing (AM), commonly referred to as 3D printing, offers the ability to not only fabricate geometrically complex lattice structures but parts in which lattice topologies in-fill volumes bounded by complex surface geometries. However, current AM processes produce defects on the strut and node elements which make up the lattice structure. This creates an inherent difference between the as-designed and as-fabricated geometries, which negatively affects predictions (via numerical simulation) of the lattice's mechanical performance. Although experimental and numerical analysis of an AM lattice's bulk structure, unit cell and struts have been performed, there exists almost no research data on the mechanical response of the individual as-manufactured lattice node elements. This research proposes a methodology that, for the first time, allows non-destructive quantification of the mechanical response of node elements within an as-manufactured lattice structure. A custom-developed tool is used to extract and classify each individual node geometry from micro-computed tomography scans of an AM fabricated lattice. Voxel-based finite element meshes are generated for numerical simulation and the mechanical response distribution is compared to that of the idealised computer-aided design model. The method demonstrates compatibility with Uncertainty Quantification methods that provide opportunities for efficient prediction of a population of nodal responses from sampled data. Overall, the non-destructive and automated nature of the node extraction and response evaluation is promising for its application in qualification and certification of additively manufactured lattice structures.

1. Introduction

Lattice structures typically refer to a form of cellular solid where an interconnected network of struts form the faces and edges of a unit cell [1]. In this research, lattice unit cells and struts are arranged periodically as opposed to stochastically. A lattice's physical behaviour is governed by its design parameters, such as: unit cell topology, unit cell geometry and strut diameter. Full control over these design parameters has recently been enabled by developments in additive manufacturing (AM) processes [2]. Therefore, AM of lattice structures have garnered interest in many applications due to the combination of these customisable design parameters and the ability of AM to fabricate lattices which conform to geometrically complex bounding surfaces [3]. Applications of these parts range from: novel heat exchangers [4,5] and auxetic lattice structures for blast and impact protection [6–8] to scaffolds for modulation of human-tissue regeneration [9].

* Corresponding author at: RMIT Centre for Additive Manufacture, RMIT University, Melbourne, Australia.
E-mail addresses: bill.lozanovski@rmit.edu.au (B. Lozanovski), martin.leary@rmit.edu.au (M. Leary).
[1] www.additivebiomanufacturing.org.

https://doi.org/10.1016/j.addma.2020.101593
Received 28 June 2020; Received in revised form 2 August 2020; Accepted 1 September 2020
Available online 12 September 2020

Metal AM processes, such as powder-bed fusion (PBF) processes, facilitate the fabrication of lattices from metallic materials with strut diameters that can exist on the micro -to meso-manufacturing scales [10]. A noteworthy application of metal AM lattice structures is their use as patient-specific orthopaedic implants [11]. Traditional solid metallic implants can lead to *stress shielding*, which refers to bone resorption in implant adjacent regions, a phenomenon primarily caused by the non-uniform stress distribution between the implant and implant-adjacent bone. The non-uniform stress distribution is caused by the high stiffness of the solid metal implant relative to that of natural bone [12–14]. Lattice customisable design parameters and metal AM offer the opportunity to fabricate lattice implants which mimic the stiffness of bone, from metals with well-known biocompatibility characteristics such as Ti6Al4V, cobalt-chromium (Co-Cr) and stainless steel 316L [14].

In applications such as lattice-structured orthopaedic implants, especially those which are load-bearing, predicting the lattice implant's mechanical properties is of utmost importance to ensure the patient-specific implant meets its mechanical/structural design criteria (e.g. bone mimicking stiffness and adequate strength for failure avoidance). Analytical approaches such as traditional force methods and Maxwell's Stability Criterion are simple predictive tools which can be applied during design to gain insight into the expected mechanical behaviour of the lattice [16–18]. One of the most notable methods of predicting the physical properties of a lattice structure is the use of the Gibson-Ashby model. The model displays the power-law dependence of a lattice's Young's Modulus and other physical properties on its relative density. Research has already been conducted on the model's accuracy for predicting the mechanical properties of SLM manufactured lattice structures [2,19,20]. However, during AM fabrication defects are produced on the fundamental strut and node elements (strut intersections) of the lattice. Fig. 1 displays nodal surface defects in Ti6Al4V Face-centred cubic lattices with ZXY-struts (FCCZXY) fabricated via selective laser melting (SLM). This causes a discrepancy between the fabricated lattice and it's idealised CAD model (used as input for AM); defects include porosity, dimensional inaccuracies and surface defects [21]. Consequently, the simple predictive methods are restrictive due to their assumptions of material homogeneity and defect-free fabrication [22]. Echeta et al. [23] have extensively reviewed PBF manufacturing defects which occur in lattice structures during fabrication. Additionally, the reader is also encouraged to explore the following literature discussing manufacturing defects in metal AM lattices: [24–28].

More complex numerical methods, such as the finite element method (FEM), are required for a more detailed analysis that includes the effects of stress concentrations caused by manufacturing defects. Currently, there exist multiple approaches to the inclusion of AM defects in lattice FE models, with many focused-on defects and dimensional inaccuracies in a lattice's strut elements. Generally, the quality of an as-manufactured lattice's struts (for a given material) is dependent on their build inclination angle, the relative density of the lattice, and the gradient direction (in cases of density graded lattice structures) [22,24,25,29]. High surface roughness on as-manufactured struts occur consistently and can be considered a defect. Phenomena such as stair-stepping and partially melted powder particles contribute to this; commonly a higher surface roughness is exhibited in the downward-facing strut surfaces (with respect to the build direction) due to the lack of support by previously melted layers and conduction to the baseplate, resulting in larger melt pools and thereby an increase in partially melted powder particles [29]. Research on the difference in mechanical behaviour between an AM lattice's nodes and its idealised CAD model has remained relatively unexplored.

1.1. Image-based finite element analysis of additively manufactured lattices

The most direct approach to the inclusion of all manufacturing defects in FE models is the use of X-ray micro-computed tomography reconstructions (μCT) of fabricated lattices as input geometries. X-ray micro-computed tomography (μCT) is a non-destructive imaging method that is increasingly used in additive manufacturing, being especially popular for evaluation of dimensional accuracy and porosity [30]. It is also useful for analysis and inspection of complex biomimetic and lattice designs [31,32]. The method makes use of a beam of X-rays passing through an object, creating a 2D projection (absorption) image. This is repeated for many angles around the object, the recorded projection images are then used to reconstruct a 3D volumetric dataset, typically using a filtered backprojection algorithm [33]. Processing of the acquired 3D data then allows virtual cross-sections revealing internal details of the object in any orientation and allows 3D volumetric measurements to be performed such as pore volume or shape, for example. It is also more widely used in materials sciences [34] and has industrial applications as summarized in [35].

One of the less widely known uses of X-ray tomography is to take actual geometries of scanned objects as input for simulations, which is also known as image-based simulation. This allows the incorporation of irregular geometries or surface deviations and internal pores into the simulations and hence provides a more accurate representation of the response of the material in question, compared to the simulation of the idealized design. For this to be useful, the method requires the acquisition of robust and high-quality μCT data.

The quality of μCT data acquisition is a factor of resolution and scan quality. Resolution is most often reported as voxel size (voxel = volumetric pixel). For sufficient resolving power for fine features typically requires at least 3 voxels across the feature, i.e. in this work the 35 μm voxel size translates to minimum detectable feature sizes of ~100 μm. The scan quality is something that is often ignored and is critically important, due to the wide variety of μCT systems, wide variety of scan parameters that can be used (voltage, current, beam filters, magnification, etc.) and the wide variety of image artefacts that can degrade image quality [36]. Some generic guidelines for μCT setup and parameter

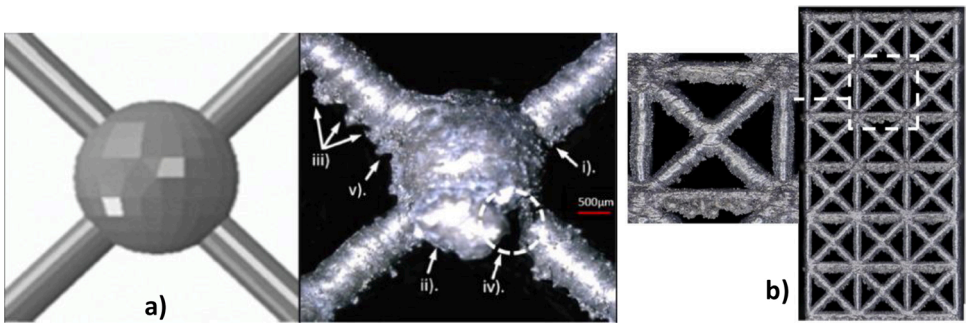

Fig. 1. Research of Alghamdi et al. [15] displaying: a) variation between designed and SLM- manufactured lattice nodes and b) surface roughness and defects in FCCZXY nodes.

choices are given in ASTM E1570-11 [37] and more recently for additively manufactured coupon samples also in [38]. However, no generic scanning guidelines are available yet for lattice or cellular structures.

Xiao et al. [39] recommended the use of μCT reconstructed lattice geometries for FE modelling to account for surface irregularities caused by the AM process. Du Plessis et al. [40] performed numerical simulations of SLM-fabricated rhombic and diagonal lattices undergoing compressive loads (Fig. 2a) and c)). Their simulations used lattice geometries derived by μCT reconstructions, results displayed the increase in Von Mises stress due to surface roughness and dimensional inaccuracies – stress concentrations highlighted in this way correlated well with cracks in samples subjected to static compression loading. Amani et al. [41] used μCT to study surface defects and porosity in two AlSi10Mg FCC lattices fabricated via SLM. A μCT-based FE model (Fig. 2a) was constructed including the effects of void nucleation and growth with a Gurson-Tvergaard-Needleman (GTN) model. GTN model parameters were sourced from Tvergaard [42] and Petit et al. [43]. A constant initial void volume fraction (f_0) was used in the homogenous GTN model, conversely, the heterogeneous model specifies each specific tetrahedral element's f_0 based upon micro porosity data gathered from μCT. Results from both GTN models were compared to those utilising a non-porous J2 plasticity model, the heterogeneous GTN model was the most accurate predictor of fracture location and stress concentrations at lattice nodes.

The direct approach of μ CT-based FEM typically requires computationally intensive continuum element meshes (e.g. tetrahedral, hexahedral elements etc.). This leads to larger restrictions in the number of unit cells able to be modelled for the analysis to be computationally feasible [44,45]. Another factor which increases total computation time is the evaluation of discretisation error (error due to an overly coarse FE mesh), generally, it is accomplished by iteratively refining the FE mesh and assessing the convergence of a critical resultant field variable to within a pre-defined tolerance or stopping criterion [46]. The process itself is known as a *mesh refinement study* or *mesh convergence test* and is completed during the *calculation verification* stage of the *Verification* and *Validation* process (V&V) [47]. Additionally, the µCT-based FEM approach requires part fabrication reducing its feasibility as Design for Additive Manufacturing (DfAM) tool. Especially during rapid prototyping or applications such as Just-In-Time manufacture of patient-specific implants [48].

Beam elements offer an alternative to computationally expensive continuum elements, though extra work is required during the prescription of beam element parameters (i.e. cross-sectional profile) to accurately depict an AM strut's mechanical behaviour [49]. The two main approaches to deriving more accurate beam parameters are geometrical characterisation or an experimental/numerical approach. The first approach uses measurements made on fabricated struts to derive equivalent beam element parameters, the second approach uses numerical or experimental analysis on fabricated struts to derive beam element parameters [50,51].

Numerous research studies have been conducted which characterise the dimensional inaccuracies in AM fabricated lattice structures enabling the geometrical approach to the specification of increased accuracy beam element parameters. Lei et al. [52] used µCT to analyse geometrical imperfections in SLM manufactured lattice structures. The image-based measurements of the as-manufactured lattice's struts enabled distributions of strut geometrical properties to be found. The distributions were used in lattice FE models via the random specification of beam element parameters (Fig. 3). Additionally, the average of the measured strut diameters was also used in the research.

Weißmann et al. [21] measured surface quality and the geometrical difference between the designed struts and those fabricated via selective laser melting (SLM) and electron beam melting (EBM). Measurements were performed using 3D digital laser scanning and digital microscopy. Alghamdi et al. [15] studied correlations between thermal simulations of SLM strut fabrication and compared it to experimental measurements of surface roughness. Regression analysis displayed predictions of surface roughness could be made with both simulated fabrication temperature as well as strut input design parameters. Alghamdi et al. [53] also studied the change in circularity and ratio of effective to nominal diameter (via μ CT), of SLM fabricated struts with varying cross-sectional design, diameter, build inclination angle and material.

The representation of as-manufactured nodal geometry in beam-based lattice FE models is a challenging undertaking. An increase in diameter or material stiffness in beam elements adjacent to node regions has been previously applied to account for effects such as material accumulation at node regions which is typically seen in fabricated lattices. Fig. 3 displays a representation of these beam elements within node regions by Mines [54]. Smith et al. [44] used beam-elements to model the compressive response of lattices with body-centred cubic and body-centred cubic with Z-strut unit cell topologies (BCC and BCCZ, respectively). To account for material aggregation and lack of contact at lattice nodes, beam element diameters adjacent to nodes were prescribed an approximately 20 % larger diameter (from 0.185 mm to 0.23 mm). Similarly, Labeas and Sunaric [55] increased beam element diameters in nodal adjacent elements by 40 %. Luxner et al. [45] increased stiffness by a factor of 1000 in nodal adjacent elements to account for material aggregation. Crupi et al. [56] increased beam element diameters in nodal regions by approximately 22 % to account for lack of contact in this region and increased material selection.

Lozanovski et al. [57] also utilised beam elements in full-scale lattice simulation. Their research included strut-level defects and modelled lattices with and without the arbitrary 40 % diameter increase in node adjacent beam elements (as per Labeas and Sunaric [55]). The beam model outputs displayed a Young's Modulus and yield strength in

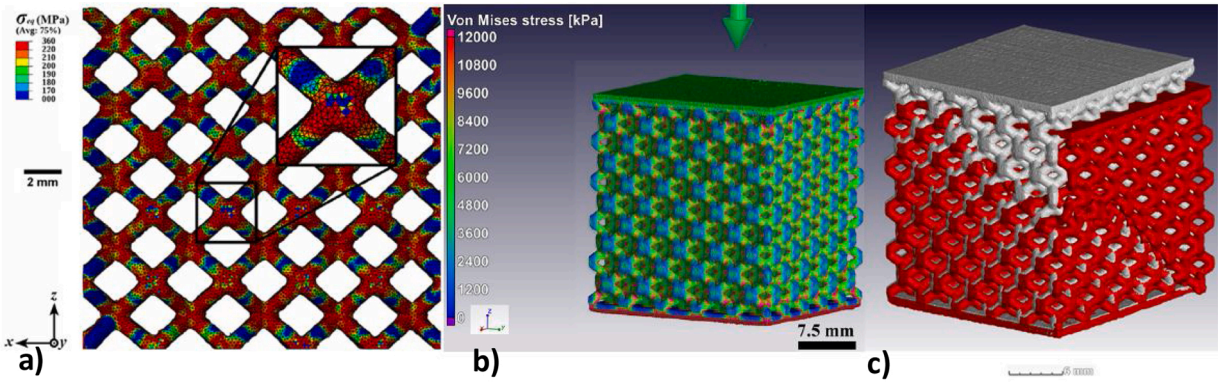

Fig. 2. µCT-based numerical simulations of AM: a) FCC lattice structure with heterogenous Gurson-Tvergaard-Needleman (GTN) material model [41] and b) rhombic lattice structure with linear elastic material model [40]. Also displayed, c), is µCT geometry of the as-fabricated rhombic lattice (white) overlayed with the geometry post-compression testing [40].

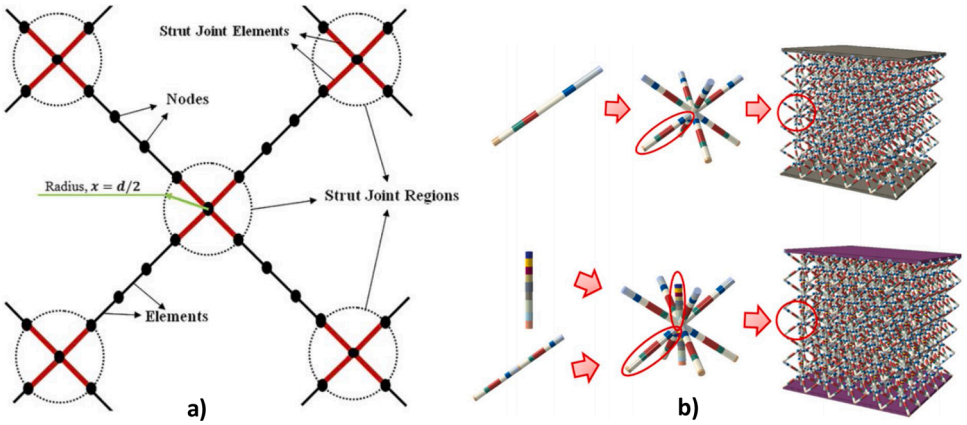

Fig. 3. a) Representation of beam-elements ('Strut Joint Elements') in lattice nodal regions ('Strut Joint Regions'), extracted from [54]. b) The random specification of beam element parameters (differentiated by colours) in a BCC and BCCZ lattice model, adapted from [52]. The combination of these two modelling techniques may further improve their accuracy and enable the quantification of uncertainty in a lattice's mechanical performance.

bending-dominated lattices that was more sensitive to the enlarged node adjacent element diameters when compared to the *stretch-dominated* lattices. This was attributed to the different deformation behaviours as *bending-dominated* lattices deforming via generated bending moments at nodes and *stretch-dominated* deform via induced axial compressive or tensile loads in struts. Overall, their research showed the requirement for sufficient nodal modelling, especially in *bending-dominated* lattices. De Galarreta et al. [49] presented a framework for constructing accurate and validated FE models, their research also displays the differences in the mechanical response of *bending-dominated* lattice's modelled with 20 % and 40 % diameter increases at elements adjacent to the nodes. Also displayed is the importance of nodal modelling as the strut diameter-to-length ratio increases.

There is currently an abundance of research focused on the experimental and numerical simulation of bulk AM lattice structures and their associated strut elements. However, there is currently little which focus on the local mechanical response of the second fundamental component of the lattice, the nodes or strut intersections. The effect of defects produced on the nodes during AM is generally reported on a unit cell scale, for example during the computational homogenisation process. Liu et al. [58] compared the homogenised Young's Moduli for as-designed and as-manufactured lattice unit cells, displaying the reduction in modulus for the as-fabricated unit cells. Refai et al. [59] studied the homogenised properties of as-designed lattice unit cells which are commonly utilised, the research did not report on any individual node's mechanical response. Dallago et al. [27,60] studied the mechanical response of as-manufactured unit cells in a cubic unit cell lattice structure fabricated via SLM. The representative volume element (RVE) geometry was centred at the nodes of the cubic unit cell. A total of eight geometries were sampled from CT data of the fabricated lattice and the FEM derived elastic modulus in a single direction (z-axis) was compared to the as-designed. The research displayed the possible variation in Young's Modulus from nodes within the same lattice structure.

In this research, the variation in the mechanical response of as-manufactured lattice nodes is studied for every node in a fabricated experimental lattice. Image-based finite element analysis is used to obtain predictions of stiffness and maximum von Mises stress. Three different load cases are prescribed to every single strut intersecting an individual as-manufactured node, representing an: axial, bending and lateral applied load. Nodes are classified based on their location in the lattice and how many struts intersect them, and struts are classified based on their build inclination angle. This research aims to study the variation in the mechanical response of an as-manufactured lattice node on an intersecting strut scale, the first of its kind.

2. Methods

Limitations of the current literature regarding the numerical simulation of as-fabricated AM nodes include the study of an AM lattice's nodes mechanical response only during bulk lattice modelling or during computational homogenisation procedures for obtaining effective unit cell properties. This research proposes a novel methodology for investigating the mechanical behaviour of nodes in AM lattice structure on a local intersecting strut level. Fig. 4 displays the general steps of the method, and it can be used in a wide variety of applications, such as the analysis of stress concentrations; comparison of the effect of nodal defects in lattices built using different AM processing parameters or machines; local node mechanical response variation and the development of more accurate lattice beam element FE models via the specification of realistic parameters in nodal adjacent beam elements. The proposed approach of nodal defect modelling is separated into seven different steps: experimental lattice design, lattice additive manufacture, X-ray μ CT, reconstruction and thresholding, geometrical isolation of lattice node elements, automated image-based FEM and statistical analysis.

2.1. Experimental lattice design

The analysis of as-manufactured nodes first requires an experimental lattice design. The lattice's design should be such tailored to the analyst's available software tools and abilities. This ensures simple automated isolation of individual nodes geometry from CT data of the manufactured lattice. The method of isolating nodes in this research utilises the periodic nature of the lattice's cross-section (Section 2.5), therefore experimental lattices can consist of commonly used unit cell topologies such as the body-centred cubic (BCC) and face-centred cubic (FCC) and their z- or axial- strut variations (BCCZ and FCCZ, respectively); the octet-truss and diamond unit cells; the combined face- and body-centred cubic (FBCC). The experimental lattice design should also consider the types of nodes found in the lattice and the aim of the study, as intersections can differ based-on characteristics such as the number of intersecting struts, differing strut diameters (as in gradient lattice structures), various intersecting strut build inclination angles, the spatial location of the node, etc. As µCT (Section 2.3) is used as an imaging technique, a minimum desired resolution must be accounted for when designing the experimental lattice structure.

In this research, the proposed method's experimental lattice design is demonstrated for a regular-FCCZ lattice with $4 \times 4 \times 3$ unit cell repetitions, Table 1 displays the lattice dimensions. Its geometry, for additive manufacturing input, is represented by a CAD model in stereolithography file format (STL) and is generated programmatically using the method of McMillan et al. [61]. The FCCZ unit cell topology

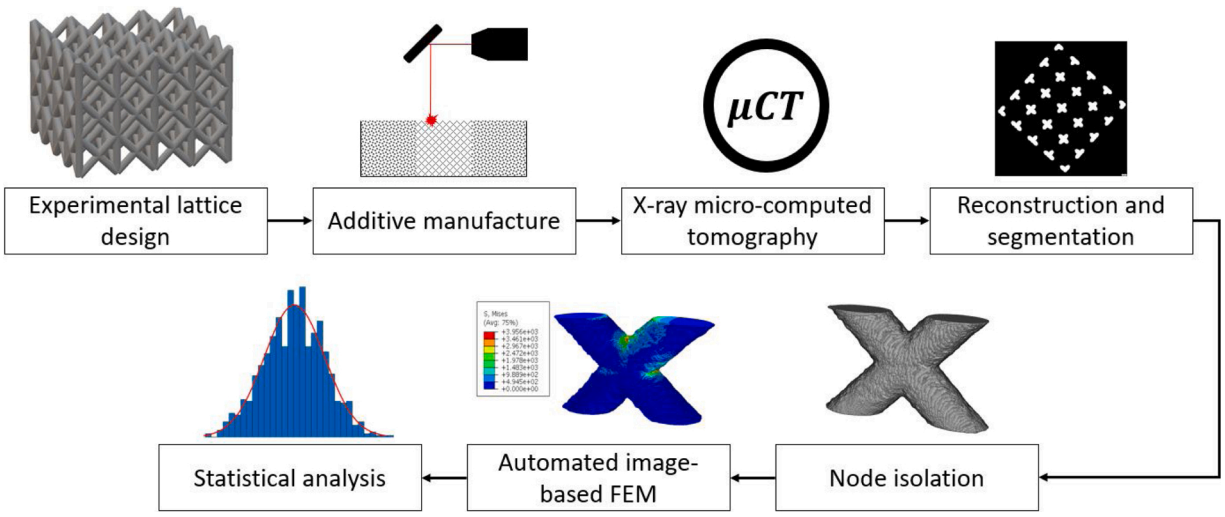

Fig. 4. The proposed methodology for investigating the mechanical response of an AM lattice's nodes.

Table 1
Overview of lattice geometry.

Lattice dimensions				
Topology	Cell size (*mm*)	Strut diameter (*mm*)	Num. Cells [X, Y, Z]	Size (*mm*) [X, Y, Z]
FCCZ	[10,10,10]	2	[4,4,3]	[40,40,30]

inherently contains struts at two different inclination angles, 45- and 90-degrees. The bulk lattice is comprised of four distinct node intersections, the: *External Lattice Corner (ELC)*, *External Lattice Face (ELF)*, *Cell Wall (CW)* and *Internal Cell Edge (ICE)*. Fig. 5 displays the experimental: bulk lattice, unit cell topology and chosen distinct nodal intersections. This research excludes nodes at the uppermost and lowermost XY-plane as they do not represent fully formed nodes and are affected by part post-processing.

2.2. Additive manufacture

Fabrication of the experimental lattice structure (Section 2.1) is dependent on the manufacturing technology of interest. In the case of AM, the manufacturing method is independent of any AM technology, machine or process category. The experimental lattice designed in this research is manufactured via SLM, a PBF-process [61]. The SLM process follows the typical layer-wise fabrication seen in other AM processes and iterations of the following form the final lattice part:

1 Deposition of metallic powder across a previously solidified layer or build platform, in an inert atmosphere maintained by an argon gas flow.
2 Programmed delivery of laser-based energy source to the surface of the metallic powder bed, contouring to a slice of the lattice's geometry.
3 Build platform lowering for subsequent layer processing.

The lattice is built from titanium alloy Ti6Al4V in an SLM Solutions 500 H L machine, which utilises fibre lasers as an energy source. The lattice is built directly on the build platform with no support structures and the lattice was oriented such that the axial or Z-strut's longitudinal axis is parallel with the build direction. Therefore, within the lattice struts are built at an inclination angle of 90 ° and 45 °. Specific processing parameters are detailed in Table 2.

2.3. X-ray micro-computed tomography

The proposed methodology requires isolation and extraction of as-fabricated lattice node geometries. This is achieved via μCT scanning

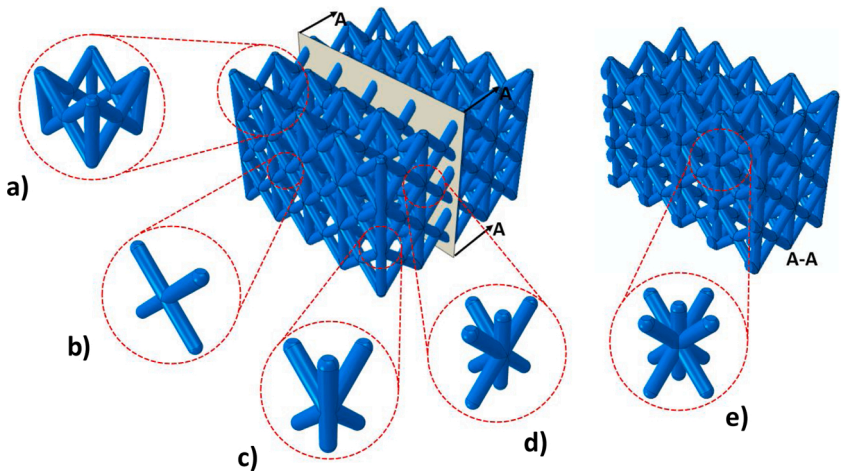

Fig. 5. FCCZ lattice and associated section view, with insets displaying: a) unit cell, b) *Cell Wall* (CW) node, c) *External Lattice Corner* (ELC) node, d) *External Lattice Face* (ELF) node and e) *Internal Cell Edge* (ICE) node.

Table 2
Overview of SLM processing parameters used in this research.

Processing parameters			
Layer thickness (μm)	60	Scan speed perimeter (mm/s)	1150
Laser power perimeter (W)	240	Scan speed infill (mm/s)	1200
Laser power infill (W)	185	Hatch spacing (μm)	105

of the AM fabricated lattice component. Scan parameters such as resolution are dependent on the size of the experimental lattice. The best possible resolution is limited by the size of the sample as the entire sample must typically fit in the field of view of the scan – typically a factor of 1000 is applicable (e.g. 35 mm sample results in 35 µm voxel size). For minimizing artefacts, the object must be mounted at an angle to the beam to allow maximum variation of beam cross-sectional directions relative to all planes – this is especially true for lattice structures, in order to limit penetration artefacts along certain directions. This and other steps in the process are not standardized and depend strongly on the equipment used, the skill and experience of the CT operator and the lattice structure material and its design.

In this research, a Bruker Skyscan 1275 machine is used for µCT scanning. The energy source operated at a voltage of 100 kV and an intensity of 100 μA with a 1 mm Cu filter applied on incident X-rays. A voxel size of 35 µm was set with energy source parameters which produce a minimum and maximum attenuation of 10–20 % and ~95 %, respectively. Scan output data is a 360-degree view image dataset (.tif format). During scanning, the experimental lattice (Section 2.1) is oriented in a manner which enables easier post-processing of cross-sectional image dataset which display the lattice's periodicity. An overview of the CT scanning parameters is visible in Table 3.

2.4. Reconstruction and segmentation

The proposed methodology requires a binarised lattice cross-sectional image dataset, which is generated during CT post-processing. Reconstruction refers to the conversion of the µCT scan acquired 2D image dataset to 3D volumetric data. Reconstruction is typically performed in software supplied with the µCT machine and is based-on variations of a filtered back-projection algorithm [30]. Segmentation is performed to separate each lattice greyscale cross-sectional image slice into image objects (either air or lattice material). The simplest form of image segmentation is thresholding, which uses a threshold value to specify if a pixel belongs to the defined image object. An example of an isolated *Cell Wall* node binary image dataset is visible in Fig. 6 alongside a volume rendering of that dataset.

As per the imaging of the fabricated lattice, the chosen methods of reconstruction and segmentation are dependent on the skill and experience of the CT operator or analyst, as well as the experimental lattice's design and fabricated material. Reconstruction in this research is completed with the proprietary software N-Recon (Micro Photonics Inc) with beam hardening and ring artefact corrections ignored. Post-processing of the greyscale cross-sectional image dataset is completed using Dream3D and ParaView, both of which are open-source image processing software. The greyscale image dataset is transformed into a binarized image dataset using the Robust Automatic Thresholding Selection (RATS) algorithm [62].

2.5. Node isolation

The geometry of every individual node in the experimental lattice is isolated and extracted from the acquired binary lattice cross-sectional image dataset. The method of isolating and extracting geometry can be completed manually via obtainment of node volume-of-interest (VOI's). The VOI refers to a stack of planar region-of-interests (ROI's), which are closed polygons specifying the node's geometry on a specific binary cross-sectional image. However, the manual approach to nodal isolation may take an excessive amount of time depending on the total number of nodes within the lattice. An alternative is the development of custom algorithms for an automated approach to node isolation.

In this research, a custom algorithm developed in MATLAB (MathWorks, 2019) is used to automatically isolate and classify every node (Fig. 5) within the experimental lattice design (Section 2.1). The algorithm utilizes the periodicity seen in the number of objects per image in the binary cross-sectional dataset. The algorithm is described in detail in the work of Lozanovski et al. [63]. However, in this research, the method is modified to include the struts which intersect the isolated node. The definition of where a node ends and a strut begins was in previous research determined by the CT cross-section data as the slice where all converging/diverging struts appear as distinct regions. This

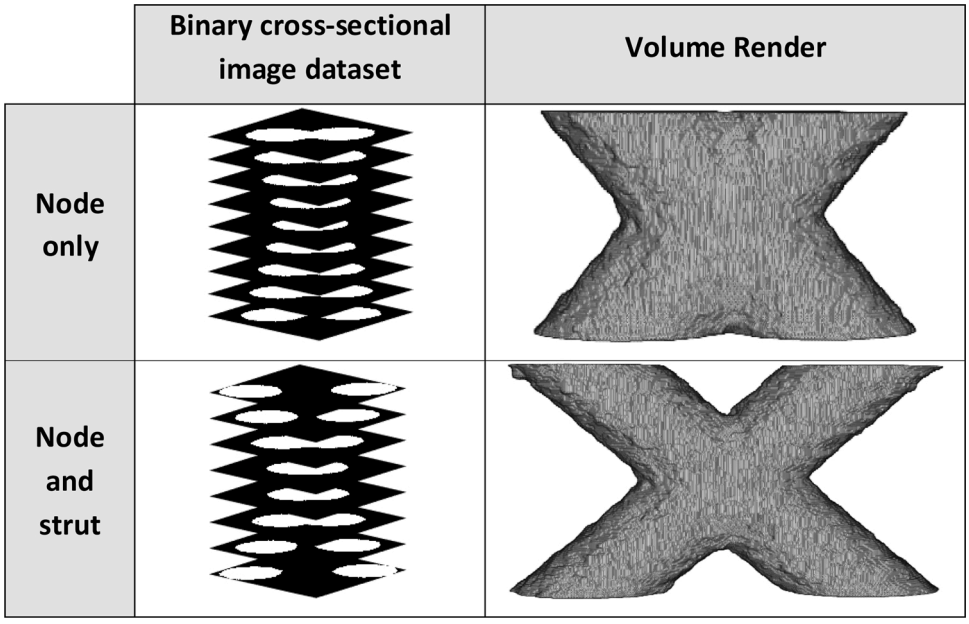

Fig. 6. The difference between a *Node only* geometry and *Node and strut* geometry. Displayed are binary cross-sectional image stack isolated from X-ray micro-computed tomography scans alongside volume renderings.

definition is dependent on the orientation of the lattice in the scanner and the direction of reconstruction slicing. For consistency, all struts which intersect an isolated node are first trimmed at the neighbouring nodes which they also connect to. They are then trimmed once more to have equal lengths measured by the z-direction component of their length (longitudinal). The difference between node only geometry and node with strut geometry is seen in Fig. 6.

For this research, the slicing aligns with build direction. The choice of appropriate strut lengths for modelling nodes and struts was considered as a length sufficiently distant from the node to avoid changing the resultant node stress field. The shortest distance to a neighbouring node gives the upper bound of the strut length. However, the length and geometry of peripheral cross-section are dependent on the goals and parameters of interest in the subsequent FE analysis of the individual nodes.

2.6. Automated image-based FEM

Automated image-based numerical modelling of each isolated node allows for the predictions of mechanical, thermal, fluid and electromagnetic properties. The FE models' characteristics are dependent on the desired solution or property-of-interest, including solution technique, meshing strategy, element type and boundary conditions. In this research, the mechanical response of the node is of interest and how it differs from its idealised CAD model used as input for AM. A linear-elastic FE model is constructed for every strut that intersects an isolated node, equating to a total of 900 FE models. Each model consists of three different loading conditions applied to an intersecting strut, achieved using three linear perturbation analysis steps and a reference base state.

Voxel-based FE meshes are generated for every isolated node via a custom-developed MATLAB algorithm and consist of reduced-integration hexahedral elements (C3D8R). In this approach, every CT voxel (0.035 mm) is represented by a single hexahedral element with a scaled Jacobian ratio of 1.0. Fig. 7 displays an *Internal Cell Edge* node's: binary image dataset; a volume rendering of the binary image with inset displaying surface roughness; generated FE mesh with inset displaying porosity on a Z-strut (Table 3).

Peripheral strut cross-sections are used as load surfaces for the application of loads and boundary conditions (Fig. 8). Each FE model represents a single strut intersecting an isolated node undergoing three different loading cases. All load cases consist of a displacement with a magnitude of 0.1 mm applied to a reference node located at the centroid of the strut's load surface (Fig. 8). FE nodes which lay on the load surface

Table 3
Micro-computed tomography scan process and post-processing parameters.

CT scanning parameters			
Filter	Cu (1 mm)	Rotation Steps (°)	0.4
Source voltage (*kV*)	100	Source current (μA)	100
Averaging (*frames*)	2	360-degree scanning	Yes
Random movement	Off	Image pixel size (μm)	35

are rigidly coupled to the reference node and all FE nodes located on other intersecting strut load surfaces are fully constrained. The three load cases are described in Table 4, and the displacement unit vector ($\hat{v}_1$) for load case 1 is calculated by:

$$\hat{v}_1 = \frac{(C_{RP} - C_{NC})}{|(C_{RP} - C_{NC})|} \tag{1}$$

where C_{RP} is the Cartesian coordinates of the generated reference point and C_{NC} is the centroid of the isolated node. The displacement unit vector for load case 3 ($\hat{v}_3$) is a vector orthogonal to $\hat{v}_1$, calculated by:

$$\hat{v}_3 = \hat{v}_1 \times \hat{v} \tag{2}$$

where $\hat{v}$ is the unit vector parallel to the build direction. The displacement unit vector for load case 2 ($\hat{v}_2$) is calculated as:

$$\hat{v}_2 = \hat{v}_3 \times \hat{v}_1 \tag{3}$$

Overall, load case 1 is aimed at simulating an axial load applied, load case 2 simulates a bulk compressive load applied to the lattice in the build direction which causes local bending at nodal intersections and load case 3 simulates a bulk compressive load applied to the lattice perpendicular to the build direction causing local lateral bending at nodal intersections. The node stiffness (k) is calculated in each load case by:

$$k = \frac{F}{\delta} \tag{4}$$

where F and δ is the magnitude of the reaction force and displacement at the reference node on the strut load surface. The maximum Von Mises stress is also evaluated in each model.

Computed stiffness and maximum von Mises stress are grouped based on the node classification (Section 2.1) as well as the build inclination of the strut to which the load is applied (e.g. ELC – 90 Degree, is the set of stiffnesses that 90-degree struts intersecting *External Lattice Corner* nodes populate). The 45 degrees struts which intersect *External*

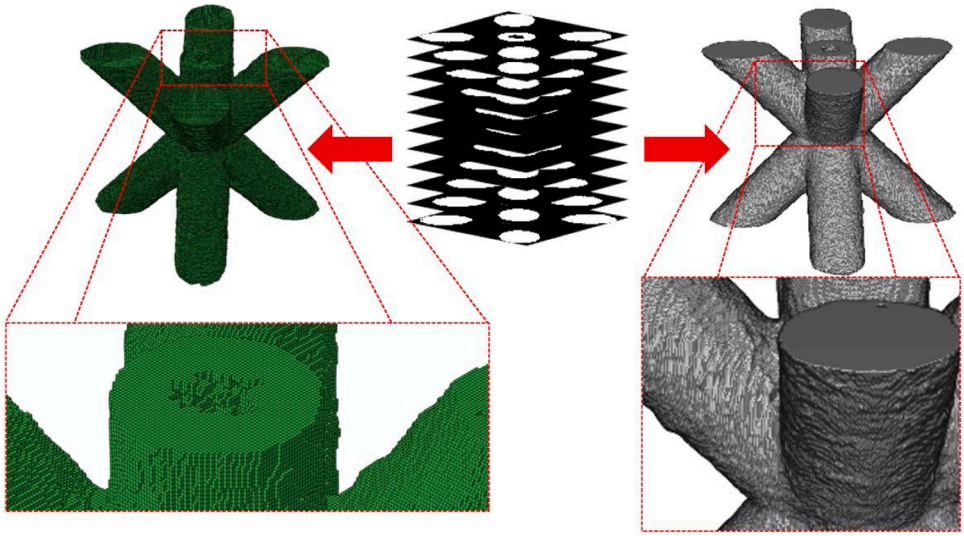

Fig. 7. Example of an *Internal Cell Edge* node's cross-sectional binary image data set being used to generate a voxel-based FE mesh and volume rendering of the as-manufactured node. Insets display magnifications of different defects visible including porosity, in the FE mesh, and surface roughness in the volume rendering. For consistency, all struts which intersect an isolated node are first trimmed at the neighbouring nodes which they also connect to. They are then trimmed once more to have equal lengths measured by the z-direction component of their length (longitudinal).

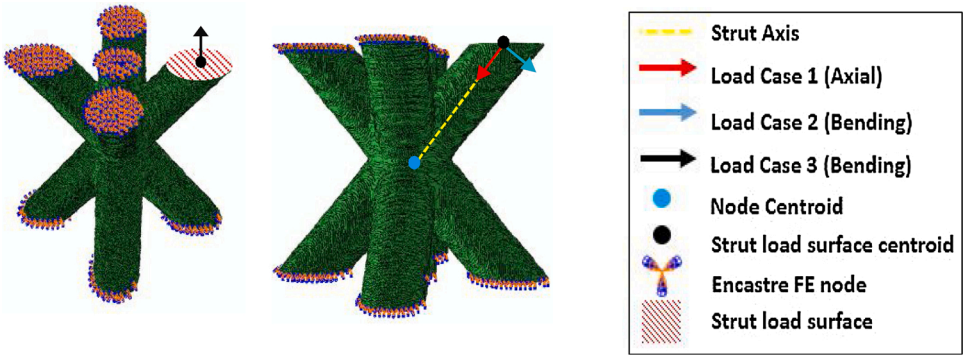

Fig. 8. Example of boundary conditions prescribed to every strut which intersects every as-manufactured node in the lattice. The three different load cases are represented by vector arrows, displaying an: axial, bending and lateral load case. For consistency, all struts which intersect an isolated node are first trimmed at the neighbouring nodes which they also connect to. They are then trimmed once more to have equal lengths measured by the z-direction component of their length (longitudinal).

Table 4
Loads and boundary conditions applied to each FE model.

Load case	Displacement (*mm*)	Location	Load Type	Description
1	0.1	Strut load surface FE nodes	Strut axis (longitudinal)	Axial Load
2	0.1	Strut load surface FE nodes	Orthogonal to strut axis	Bending
3	0.1	Strut load surface FE nodes	Orthogonal to strut axis (transverse)	Lateral Bending

Lattice Face nodes are further separated by those which have a longitudinal axis aligned parallel to the external face of the bulk lattice structure and those which do not.

Idealised FE models are developed for every individual node classification and strut inclination angle. For each combination of strut inclination angle and node classification, three different FE models are constructed. The first FE model utilises meshing of solid model representation of the isolated node. Meshes consist of either first-order reduced integration hexahedral elements (C3D8R) or, in cases where automatic meshing fails, second-order tetrahedral elements (C3D10). The second FE model consists of a voxel-based mesh of the idealised node, in which voxel dimensions match that of the μCT scans. This model aims to represent CT scanning and subsequent image-based FEM of a 'perfectly' fabricated lattice node. The final FE model uses second-order three-dimensional beam elements (B32) to represent the lattice nodes. For each node FE model, intersecting struts have lengths equal to the mean strut length of the as-fabricated nodes, and strut diameters are equal to their design (Table 1).

2.7. Statistical analysis

Statistical analysis of the automated image-based FEM results is dependent on the aim of the node study, whether that be descriptive statistics on the experimental lattice fabricated or inferential statistics for other lattices built using the same AM process and material. In this research, the aim is to utilise the stiffness results from the node numerical study (Section 2.6) in future work involving the construction of more accurate lattice-scale numerical models. This includes stochastic analysis, in which finite elements in lattice node regions have random prescribed parameters generated via sampling of a fitted probability distribution. Therefore, the selection of well-fitted statistical models is of importance. Especially when probabilistic bounds are of significance, such as in reliability and certification applications, of a selected AM process category and associated processing parameters.

In this research, the Bayesian Information Criterion (BIC) is used to select the optimal distribution from the candidate: *normal, lognormal, gamma, exponential, generalised extreme value (GEV), Rician, Birnbaum-Saunders* and *Weibull* distributions. The BIC is calculated by:

$$BIC = -2\log_e L(\widehat{\theta}) + k\,\log_e n \tag{5}$$

where $L(\widehat{\theta})$ is the maximum value of the likelihood function for the candidate distribution and $\widehat{\theta}$ are the parameters which maximize this (e.g. maximum likelihood estimators of mean and variance for normal distribution), k is the number of statistical parameters and n is the sample size.

Selection of the optimal distribution from the set of candidate distributions (*normal, lognormal, gamma,* etc.) can, in some cases, not describe the data properly. Additionally, the use of parametric distributions inherently makes assumptions about the distribution of the data. To avoid this non-parametric Kernel Density Estimation (KDE) is used to estimate the probability distributions of the nodal stiffnesses. The KDE is the estimated probability density function, $\widehat{f}_h(x)$, for a real value of a random variable, x:

$$\widehat{f}_h(x) = \frac{1}{nh}\sum_{i=1}^{n} K\left(\frac{x - x_i}{h}\right) \tag{6}$$

where $(x_1, x_2, \ldots, x_n)$ are the random samples from the actual distribution, n is the sample size, $K(\cdot)$ is the Gaussian type kernel smoothing function and h is the *bandwidth*. The *bandwidth* is selected in each case using the method recommended for Gaussian kernel functions by Bowman and Azzalini [64]. The best-fit statistical models and KDE's are evaluated for every distinct combination of load case, intersecting strut build inclination angle and node classification stiffness.

3. Results and discussion

The Results and Discussion section is divided into two subsections, the first subsection displays the variation in stiffness between the nodes and results from statistical analysis. The second subsection displays stress distributions of isolated nodes and max von Mises stress.

3.1. Lattice node stiffness

Simulated stiffness for each combination of load case, intersecting strut build inclination angle and node classification is displayed in Figs. 9, 10 and Fig. 1212 . Also displayed is percent error ($e_{load\ case}$) between the mean stiffness value of the as-manufactured and the idealised node, calculated by:

$$e_{load\ case} = 100\% \times \frac{(k_{ideal,i} - \bar{k}_{CT,i})}{\bar{k}_{CT,i}} \tag{7}$$

Where for a given load case, $k_{ideal,i}$ is the ideal stiffness for the i -th combination of intersecting strut building inclination angle and node classification. $\bar{k}_{CT,i}$ is the corresponding mean stiffness found via image-

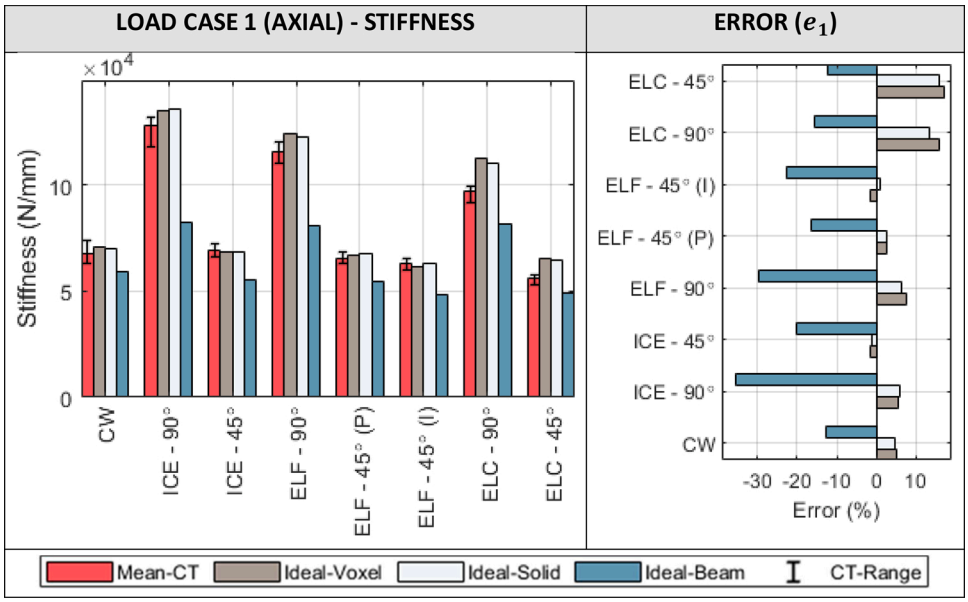

Fig. 9. The as-manufactured and idealised axial stiffness (Load case 1) for each distinct combination of intersecting strut build inclination angle and node classification. Also displayed is the percentage error between as-manufactured and idealised. Abbreviations: *Cell Wall* (CW); *Internal Cell Edge* – load applied to 90° strut (ICE - 90°); *Internal Cell Edge* – load applied to 45° strut (ICE - 45°); *External Lattice Face* – load applied to 90° strut (ELF - 90°); *External Lattice Face* – load applied to external 45° strut (ELF – 45° (P)); *External Lattice Face* – load applied to internal 45° strut (ELF – 45° (I)); *External Lattice Corner* – load applied to 90° strut (ELC - 90°); *External Lattice Corner* – load applied to 45° strut (ELC - 45°).

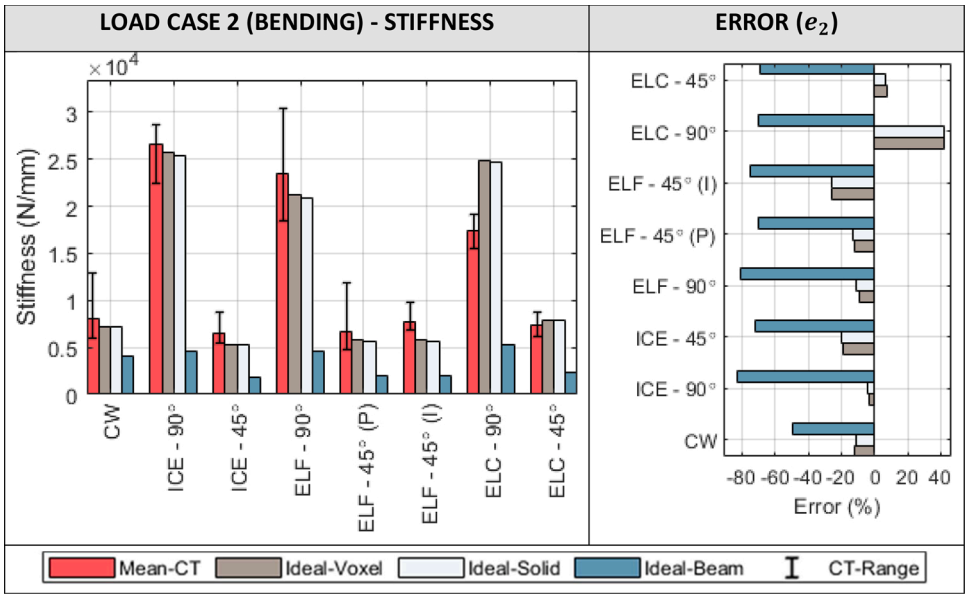

Fig. 10. The as-manufactured and idealised bending stiffness (Load case 2) for each distinct combination of intersecting strut build inclination angle and node classification. Also displayed is the percentage error between as-manufactured and idealised. Abbreviations: *Cell Wall* (CW); *Internal Cell Edge* – load applied to 90° strut (ICE - 90°); *Internal Cell Edge* – load applied to 45° strut (ICE - 45°); *External Lattice Face* – load applied to 90° strut (ELF - 90°); *External Lattice Face* – load applied to external 45° strut (ELF – 45° (P)); *External Lattice Face* – load applied to internal 45° strut (ELF – 45° (I)); *External Lattice Corner* – load applied to 90° strut (ELC - 90°); *External Lattice Corner* – load applied to 45 ° strut (ELC - 45 °).

based FEM study (Section 2.6). Stiffness results from load case 1, an axial load, show the relative inaccuracy of ideal beam element models in comparison to ideal solid and voxel-based continuum elements models. The beam element model error was –35 % and occurred in the loading of the 90 ° strut of an *Internal Cell Edge* node. In comparison, the solid and voxel models displayed a stiffness error relative to $\bar{k}_{CT}$ of 6.0 % and 5.5 %, respectively.

Axial stiffness also differs for the same intersecting strut inclination angle and node combination. The *Cell Wall* nodes only contain struts built at an inclination angle of 45 degrees and are the most abundant within the experimental FCCZ lattice (Section 2.1), with 120 individual nodes and a total of 480 FE simulations conducted (1440 individual load cases). The minimum simulated axial stiffness (63.4 kN/mm) differs from the maximum (73.6 kN/mm) axial stiffness by approximately 15 %. A variation of 15 % in the axial response of the intersecting struts, indicates a spread of defects throughout nodes which affect the nodes structural response differently.

External Lattice Corner (ELC) node, d) *External Lattice Face* (ELF) node and e) node

Solid and voxel-based idealised FE models are more accurate at representing the 45° struts axial stiffness than the 90° struts in the *External Lattice Face* nodes. This behaviour is also seen in the *Internal Cell Edge* node, however, the relative error in the *External Lattice Corner* node is approximately the same between the 45 ° and 90 ° struts.

Loading Case 2 (Fig. 10) represents a bending load applied to the 45 ° struts of the lattice nodes which mimics a that seen in a typical lattice axial compression test. The *Cell Wall* lattice nodes only contain struts built at an inclination angle of 45°, with a mean simulated bending stiffness of 8.1 kN/mm. The minimum simulated bending stiffness (5.981 kN/mm) differs from the maximum (12.917 kN/mm) by 73 %. The relatively large differences in bending stiffness are due to both to geometrical imperfections and the slightly longer struts in the minimum case. The lengths of the maximum and minimum stiffness strut load case (denominator Eq. 1) were 3.20 mm and 3.51 mm. Comparatively, the mean strut length of *Cell Wall* load cases was 3.43 mm. Fig. 11 displays the Von Mises stress distribution and of the *Cell Wall* extrema bending

stiffness cases. In general, idealised continuum-element FE models predict the bending stiffness of all node types, however, idealised beam element FE models vastly under-predict the bending stiffness of the experimental lattice's nodes.

Load case 3 represents a force applied in the strut's lateral axis direction and is aimed at simulating compression of a lattice perpendicular to the experimental lattice's build direction (Fig. 5). The error between idealised and image-based FE results are comparable to load case 2. In both load cases (2 and 3), there is a greater range of calculated stiffnesses in struts built at 90° (i.e. ICE-90°, ELF-90°, ELC-90°). These large ranges in vertical struts under bending load conditions may be in part due to the automated application of boundary conditions (Section 2.6) and the sensitivity of the nodes mechanical response to the applied load direction, as well as manufacturing defects.

3.2. Statistical models

The sample size for each strut node category is visible in Table 5 and histograms of stiffness results and their best-fit probability distributions (Section 2.7) are shown in Appendix A. The best-fit distributions and parameter estimates for every strut-node category and load case are also displayed in Table 6. These distributions can be used to generate realizations of node stiffness in future lattice scale studies. However, before using these parametric distributions some numerical artefacts should be considered. We remark on the most pertinent issues here. For the axial stiffness case (Load Case 1), the best-fit distribution for *Cell Wall* nodes was found to be a *GEV Type III*, with support $(-\infty, 8.24e{+}4]$. The use of *Generalised Extreme Value* distribution (*Type II or Type III*) limit either minima or maxima and the analyst must deem their usefulness for applications such as lattice scale Monte Carlo simulation. In the case of the *Cell Wall* axial load (load case 1), this translates to a zero probability of the stiffness exceeding the support upper bound of 8.24 kN/mm. The calculated probability of an axial stiffness occuring between the maximum found experimentally (73.6 kN/mm) and 8.24 kN/mm (GEV support upper bound) is 1.48 %. Comparatively, the probability calculated using a fitted *normal* distribution is 0.299 %. This indicates a five times higher chance of sampling a stiffness which is greater than that found experimentally with the GEV fit distribution. Therefore, the feasibility of the selected distribution, including its tails, must be considered to best suit the application of the statistical analysis.

In Appendix B we compare the cumulative distribution function (CDF) of the best fit distributions with the CDF of the kernel density estimate. We also plot the empirical cumulative distribution function (ECDF) and confidence intervals. The stiffness for *Cell Wall* nodes has the largest sample size and consequently, the confidence intervals of the empirical CDF are smaller than for the other node types (Fig. 13). The KDE of the CW stiffness is within the confidence intervals for all load cases, however, the best CDF of the best fit distribution is outside the confidence intervals for load cases 2 and 3. This suggests that the KDE is a better approximation of the data than the best fit distribution. The confidence intervals of the ECDF are largest for ICE 90-degree nodes. For this node type, the best fit distribution approximates the upper limit of the distribution better than the KDE for all load types. The most appropriate distribution (KDE or best fit) depends on how these distributions will be used in future studies. In future research, samples are to be generated from these distributions to specify effective beam element parameters in lattice nodal regions to quantify uncertainty in outputs of lattice models. This approach to lattice beam element modelling may be represented as a combination of prior lattice modelling techniques by Lei et al. [52] and Mines et al. [54]. Fig. 12 displays an extract from both of their research. This lattice modelling would also enable studies to be conducted on the effects of random defects on a lattice structure's strength. We will investigate the significance of the error in the best-fit and KDE distributions on lattice scale predictions in these future studies.

As with finite samples sizes the discretization error of the finite element models used to approximate stress can also affect the estimated distributions of node stress [13]. Due to the sheer number of high-resolution lattice node FE models (900, each with three different analysis steps), a mesh refinement study [47] for each lattice node FE model was deemed computationally infeasible, especially for nodes which had a high number of intersecting struts. However, a convergence test was performed on a *Cell Wall* node FE model (Section 2.6), in which each element (element size equals CT resolution) was split into 8 smaller elements. The refined model contained 6859304 hexahedral elements (C3D8R) and the resultant stiffness was used as a convergence metric. The difference in refined and initial voxel-based FE model (857413

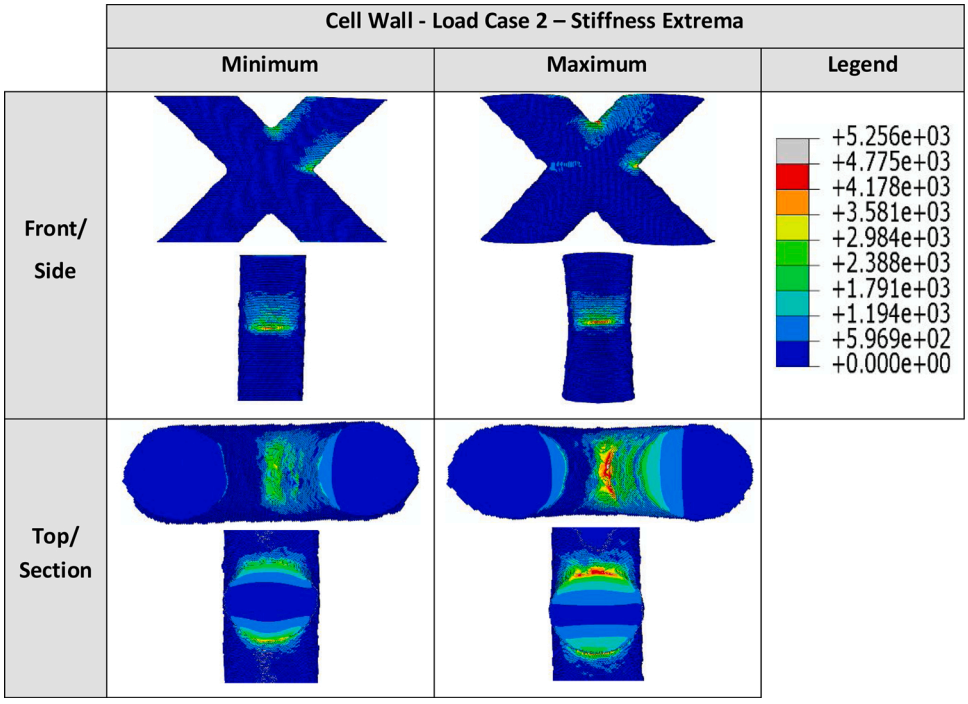

Fig. 11. Von Mises stress distribution (MPa) for the *Cell Wall* nodes found with the maximum and minimum bending stiffness (Load case 2). Abbreviations: *Cell Wall* (CW); *Internal Cell Edge* – load applied to 90° strut (ICE - 90°); *Internal Cell Edge* – load applied to 45° strut (ICE - 45°); *External Lattice Face* – load applied to 90° strut (ELF - 90°); *External Lattice Face* – load applied to external 45° strut (ELF – 45° (P)); *External Lattice Face* – load applied to internal 45 ° strut (ELF – 45° (I)); *External Lattice Corner* – load applied to 90° strut (ELC - 90 °); *External Lattice Corner* – load applied to 45° strut (ELC - 45°).

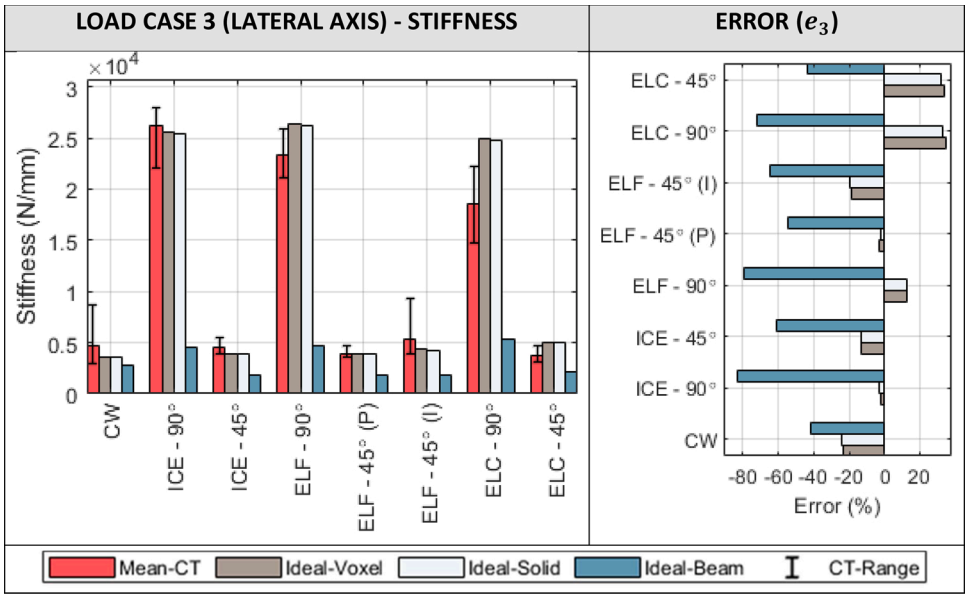

Fig. 12. The as-manufactured and idealised lateral stiffness (Load case 3) for each distinct combination of intersecting strut build inclination angle and node classification. Also displayed is the percentage error between as-manufactured and idealised. Abbreviations: *Cell Wall* (CW); *Internal Cell Edge* – load applied to 90° strut (ICE - 90°); *Internal Cell Edge* – load applied to 45° strut (ICE - 45°); *External Lattice Face* – load applied to 90° strut (ELF - 90°); *External Lattice Face* – load applied to external 45° strut (ELF – 45° (P)); *External Lattice Face* – load applied to internal 45° strut (ELF – 45° (I)); *External Lattice Corner* – load applied to 90° strut (ELC - 90°); *External Lattice Corner* – load applied to 45 ° strut (ELC - 45°).

Table 5
The sample sizes for each strut node category.

Sample Size							
Cell Wall	Internal Cell Edge 90°	Internal Cell Edge 45°	External Lattice Face 90°	External Lattice Face 45° (P)	External Lattice Face 45° (I)	External Lattice Corner 90°	External Lattice Corner 45°
480	36	144	48	96	48	16	32

Table 6
Best-fit probability distribution and associated parameters for each combination of load case, intersecting strut build inclination angle and node classification.

Node	CW	ICE- 90°	ICE - 45°	ELF - 90°	ELF-45° (P)	ELF-45° (I)	ELC- 90°	ELC - 45°
Load Case 1								
Dist. Type	GEV -Type III	GEV-Type III	Birnbaum–Saunders	Rician	GEV -Type III	Rician	GEV -Type III	Weibull
Param.	(k,σ,μ)	(k,σ,μ)	(β,γ)	(s,σ)	(k,σ,μ)	(s,σ)	(k,σ,μ)	(λ,k)
Param. Values	−0.1008, 1.6e+3, 6.654e+4	−0.124, 4.24e+3, 1.28e+5	6.928e+4, 1.805e-2	1.154e+5, 2.142e+3	−4.27e-1, 1.356e+3, 6.535e+04	6.268e+4, 1.20e+3	−1.051, 2.211e+3, 9.732e+4	5.636e+4, 5.113e+1
Load Case 2								
Dist. type	GEV -Type II	Weibull	GEV-Type II	Birnbaum–Saunders	GEV-Type II	GEV-Type III	Rician	Rician
Param.	(k,σ,μ)	(λ,k)	(k,σ,μ)	(β,γ)	(k,σ,μ)	(k,σ,μ)	(s,σ)	(s,σ)
Param. Values	0.1396, 1.055e+3, 7.375e+3	2.718e+4, 2.392e+1	4.124e-3, 4.594e+2, 6.307e+3	2.326e+4, 0.1138	0.1681, 8.128e+2, 5.955e+3	−1.18e-2, 4.672e+2, 7.478e+3	1.739e+4, 1.186e+3	7.309e+3, 7.021e+2
Load Case 3								
Dist. type	GEV-Type II	GEV-Type III	Birnbaum–Saunders	Rician	Birnbaum–Saunders	GEV-Type II	Gamma	Birnbaum–Saunders
Param.	(k,σ,μ)	(k,σ,μ)	(β,γ)	(s,σ)	(β,γ)	(k,σ,μ)	(k,θ)	(β,γ)
Param	0.6030, 7.24e+2, 3.736e+3	−0.8749, 1.641e+3, 2.608e+4	4.549e+3, 7.323e-2	2.336e+4, 1.186e+3	3.969e+3, 6.980e-2	0.7201, 4.984e+2, 4.390e+3	7.364e+1, 2.523e+2	3.760e+3, 9.717e-2

Abbreviations: *Cell Wall* (CW); *Internal Cell Edge* – load applied to 90° strut (ICE - 90°); *Internal Cell Edge* – load applied to 45° strut (ICE - 45°); *External Lattice Face* – load applied to 90° strut (ELF - 90°); *External Lattice Face* – load applied to external 45° strut (ELF – 45° (P)); *External Lattice Face* – load applied to internal 45° strut (ELF – 45° (I)); *External Lattice Corner* – load applied to 90° strut (ELC - 90°); *External Lattice Corner* – load applied to 45° strut (ELC - 45°).

hexahedral elements) for each load case was 0.202129 %, 0.234998 % and 0.294994 %, respectively. These values are much smaller than the distance between confidence intervals for all node and load types. Therefore, we conclude that the error due to discretization is insignificant when compared to the error induced by the finite sample sizes used to compute the ECDFs.

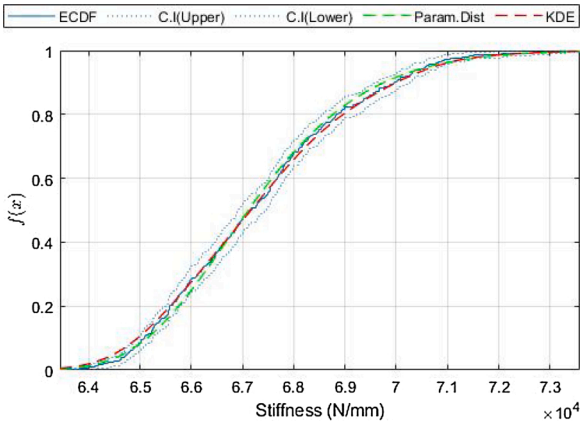

Fig. 13. *Cell Wall* (Load Case 1) stiffness empirical cumulative distribution function (ECDF) with confidence intervals. Also displayed is the best-fit parametric distribution (GEV -Type III in this case) and KDE.

3.3. Stress concentration factors

Stress concentration factors, K_t, in this work are calculated as the ratio of maximum von Mises stress in the image-based FEM results, to that calculated from the idealised geometry. To ensure the effects of element distortion are mitigated in the comparison, the voxel-based idealised model is used to calculate K_t. Fig. 14 displays the arithmetic mean stress concentration factor and maximum for each combination of load case, intersecting strut build inclination angle and node classification. The relatively large strut diameters and unit cell dimensions of the fabricated experimental lattice are normally associated with good build quality due to the small laser spot and powder size utilised in the SLM process. Therefore, the mean stress concentration factor across all node classifications and load cases are below one.

Factors which also contribute to a $K_t < 1$ for as-manufactured nodes is the increased material at edges between node intersecting struts and the dimensional inaccuracies themselves. The extra material seen at nodal intersections behave similarly to a stress reliever, like a fillet, reducing the sharp external corners seen in the as-designed node. Fig. 15 displays a volume render of *Internal Cell Edge* as-manufactured and idealised voxel-based node geometry used in calculations of stress concentration factors. Insets within the figure display the increased radius at the intersection edge of two 45 ° and one 90 ° struts in the as-manufactured geometry when compared with the idealised voxel-based geometry.

Examples of certain load cases with the maximum overall element von Mises stresses are displayed in Fig. 16. Generally, most display high-stress regions at the edge intersection of struts. Fig. 16b) displays the von Mises stress distribution for the maximum stress case of the *Internal Cell Edge*'s 90 ° -strut under axial load (load case 1). The maximum stress, in this case, occurs at the edge of an internal pore. However, the calculated stress concentration factor (Fig. 14- Max stress concentration factor) is still approximately 1. In this case, severe porosity has a similar impact on stress concentrations as the sharp corners in the as-designed node. Overall, dimensional inaccuracies between as-manufactured and as-designed may prove to be beneficial in reducing the number of stress raisers present in AM lattice's structures nodes.

It should be noted that the idealised CAD geometry has sharp concave edges which lead to stress singularities. However, we have utilised a voxel FE mesh to reduce the effects of these sharp corners. An actual 'defect-free' manufactured lattice would have edge fillets of unknown radii. At the lattice scale, the results shown in Fig. 14 indicate that the idealised lattice (with sharp edges) FE models may generally predict a lattice of lower strength.

4. Conclusions

This research demonstrates a novel methodology to non-destructively quantify the mechanical response of individual as-manufactured lattice node elements. It utilises an FCCZ-lattice manufactured from Ti6Al4V via selective laser melting to demonstrate the methodology. Micro-computed tomography (μCT) derived cross-sectional images of the as-manufactured lattice are used as input to a custom algorithm which automatically isolates the geometry of individual nodes from the μCT data of the bulk lattice. Voxel-based FE meshes of each isolated node are then algorithmically generated; allowing automated numerical analysis to generate both qualitative and quantitative data for each of the strut intersections for each node element.

In this research, the mechanical response is qualitatively reported by the von Mises stress field (for example Fig. 14) and quantified by the local stiffness and geometric stress concentration factor evaluated with respect to the idealised node geometry. Consolidating the quantitative data for each strut intersection throughout the lattice structure allows statistical analysis of the distribution of mechanical response categorised according to load type, strut inclination angle and node position (Section 2.1).

It is known that geometric defects inherent to additive manufacturing processes affect the predictive capability of FE models which are typically based on idealised geometry (Section 1.1). This is especially true for FE models which utilise more primitive structural elements, such as beam elements. By enabling the robust quantification

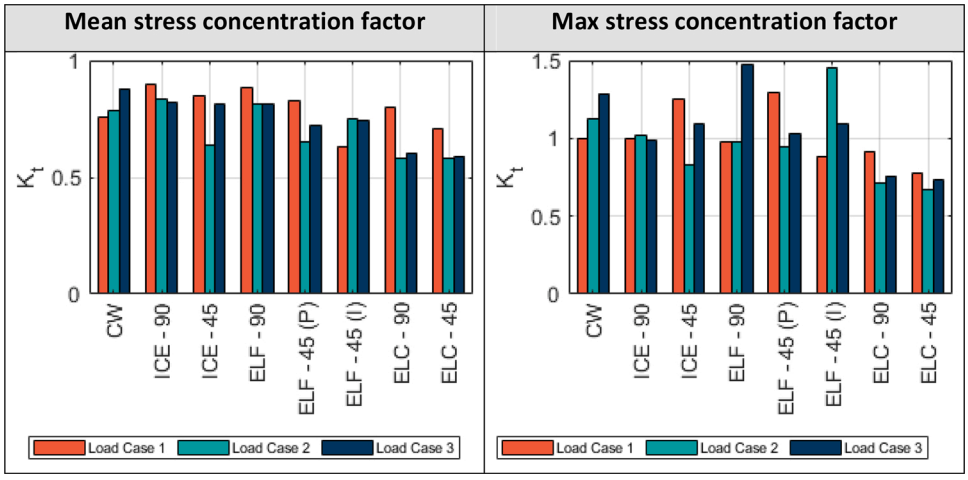

Fig. 14. Mean and max stress concentration factors for each distinct combination of load case, intersecting strut build inclination angle and node classification. Abbreviations: *Cell Wall* (CW); *Internal Cell Edge* – load applied to 90° strut (ICE - 90°); *Internal Cell Edge* – load applied to 45° strut (ICE - 45°); *External Lattice Face* – load applied to 90° strut (ELF - 90°); *External Lattice Face* – load applied to external 45° strut (ELF – 45° (P)); *External Lattice Face* – load applied to internal 45° strut (ELF – 45° (I)); *External Lattice Corner* – load applied to 90° strut (ELC - 90°); *External Lattice Corner* – load applied to 45° strut (ELC - 45°).

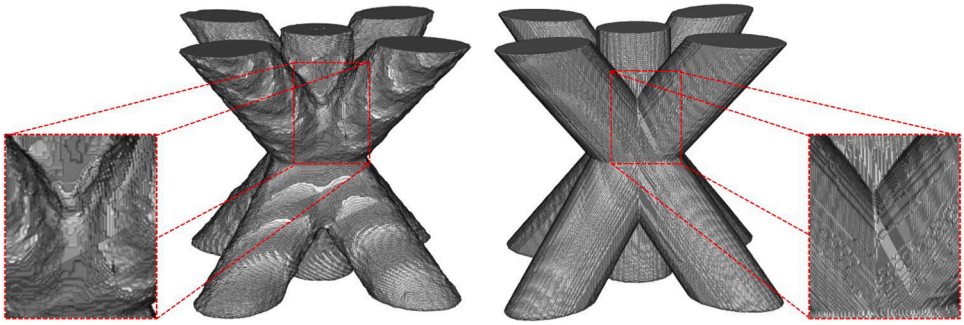

Fig. 15. As-manufactured and idealised volume renderings of an *Internal Cell Edge* node. Insets display the reduction in sharp corner radii in the as-manufactured node when compared with the idealised as-designed model.

of mechanical response in the node region, this research can enhance FE modelling of as-manufactured lattice structures.

The methodology demonstrated in this research allows for previously unavailable insight into the mechanical response of as-manufactured AM lattices structures. This insight is generated non-destructively and is therefore applicable to both the characterisation of the influence of design variables influence design variables on lattice structural integrity as well as to the certification of manufactured lattice intended for high-value applications such as medical implants and safety-critical system design.

In summary, the primary contributions of this research are:

- A robust method is proposed for characterising the structural behaviour for as-manufactured node elements within a lattice structure. This method is implemented algorithmically, enabling effective and systematic analysis of the influence of process parameters and node geometry on mechanical response.
- As the method may be applied non-destructively, it provides a systematic strategy for certification of high-value lattice systems. This outcome is especially compatible with generative methods of AM system design as it allows for algorithmic production and certification methods that enable high-value product to be manufactured at low cost.
- By quantifying the stiffness of strut elements interacting with as-manufactured geometry, this methodology provides a robust basis for correctly defining the stiffness response of interacting beam elements. This outcome allows the definition of computationally efficient beam element representations with realistic mechanical parameters.
- Novel approaches to the simulation of full-scale lattice structures are given by providing robust statistical data on the mechanical behaviour of nodes for a specified processing input and lattice topology. This outcome enables the generation of lattice node Representative Volume Elements (RVE) models in which periodic boundary conditions could be applied, as well as the specification of more accurate lean lumped parameter models which include AM defects and geometry.
- The combination of high-resolution lattice node FE models and periodic boundary conditions enables predictions of stress in as-manufactured nodes geometries without the excessive computational cost associated with the simulation of an entire lattice structure. This can be achieved in a manner like that of the research conducted by Yang et al. [65], in which both experimental and FE models show fatigue life is governed by not only surface quality but how struts are connected (nodes) and their general lattice deformation behaviour (i.e. bending or stretch dominated).

It is anticipated that the presented methodology provides a basis for the non-destructive simulation of AM node element response that can be extended in subsequent research, including effects of intersecting strut length on nodes mechanical behaviour, correlation of nodal geometric properties to their mechanical behaviour, the extension of the work to fatigue and non-linear plasticity analysis, as well as the development of custom nodal geometry with improved stiffness, strength and crack resistance.

Data availability

Binary image dataset of all isolated nodes is available in MAT file format (.mat) by request from martin.leary@rmit.edu.au.

CRediT authorship contribution statement

Bill Lozanovski: Conceptualization, Data curation, Formal analysis, Investigation, Methodology, Software, Validation, Visualization, Writing - original draft, Writing - review & editing. **David Downing:** Conceptualization, Data curation, Supervision, Formal analysis, Investigation, Methodology, Software, Project administration, Validation, Visualization, Writing - original draft, Writing - review & editing. **Rance Tino:** Data curation, Investigation, Software, Validation, Visualization, Writing - original draft, Writing - review & editing. **Anton du Plessis:** Supervision, Methodology, Validation, Visualization, Writing - original draft, Writing - review & editing. **Phuong Tran:** Conceptualization, Methodology, Supervision, Validation, Visualization, Writing - original draft, Writing - review & editing. **John Jakeman:** Formal analysis, Investigation, Methodology, Supervision, Validation, Visualization, Writing - original draft, Writing - review & editing. **Darpan Shidid:** Investigation, Methodology, Supervision, Validation, Visualization, Writing - original draft, Writing - review & editing. **Claus Emmelmann:** Investigation, Methodology, Supervision, Validation, Visualization, Writing - original draft, Writing - review & editing. **Ma Qian:** Funding acquisition, Investigation, Project administration, Resources, Software, Supervision, Validation, Visualization, Writing - original draft, Writing - review & editing. **Peter Choong:** Funding acquisition, Investigation, Project administration, Resources, Software, Supervision, Validation, Visualization, Writing - original draft, Writing - review & editing. **Milan Brandt:** Conceptualization, Data curation, Formal analysis, Funding acquisition, Investigation, Methodology, Project administration, Resources, Software, Supervision, Validation, Visualization, Writing - original draft, Writing - review & editing. **Martin Leary:** Conceptualization, Data curation, Formal analysis, Funding acquisition, Investigation, Methodology, Project administration, Resources, Software, Supervision, Validation, Visualization, Writing - original draft, Writing - review & editing.

Declaration of Competing Interest

The authors report no declarations of interest.

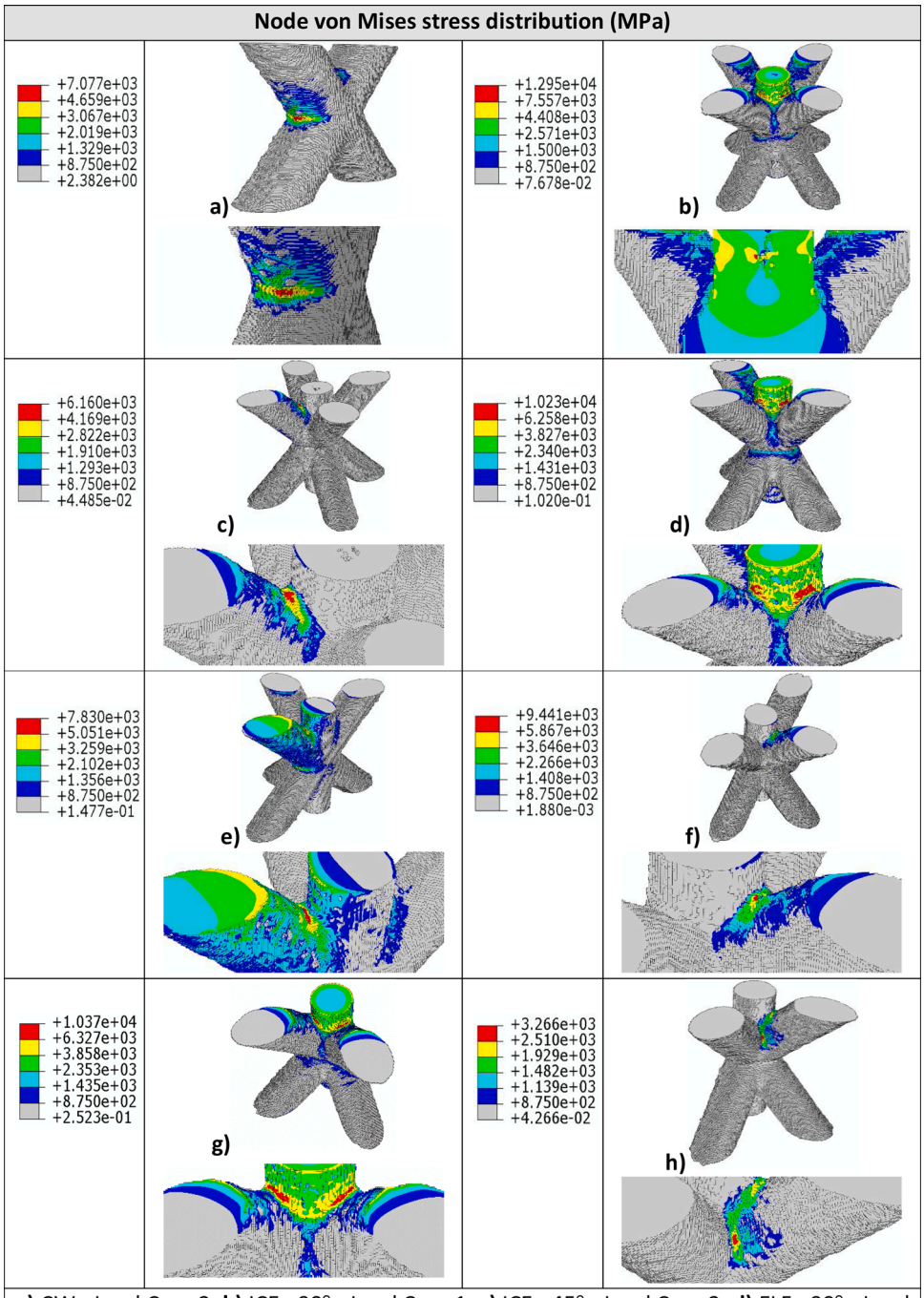

a) CW - Load Case 2, **b)** ICE - 90° - Load Case 1, **c)** ICE - 45° - Load Case 2, **d)** ELF - 90° - Load Case 1, **e)** ELF - 45°(P) - Load Case 1, **f)** ELF - 45°(I) - Load Case 2, **g)** ELC - 90° - Load Case 1, **h)** ELC - 45° - Load Case 3

Fig. 16. Examples of the von Mises stress distribution for different load cases and each combination of intersecting strut build inclination angle and node classification. Displayed combination with the resultant maximum von Mises stress. Abbreviations: *Cell Wall* (CW); *Internal Cell Edge* – load applied to 90° strut (ICE - 90°); *Internal Cell Edge* – load applied to 45° strut (ICE - 45°); *External Lattice Face* – load applied to 90° strut (ELF - 90°); *External Lattice Face* – load applied to external 45° strut (ELF – 45° (P)); *External Lattice Face* – load applied to internal 45° strut (ELF – 45° (I)); *External Lattice Corner* – load applied to 90° strut (ELC - 90°); *External Lattice Corner* – load applied to 45° strut (ELC - 45°).

Acknowledgements

The authors acknowledge the use of facilities within the RMIT Advanced Manufacturing Precinct and the RMIT Microscopy and Microanalysis Facility (RMMF). This research was conducted by the Australian Research Council Industrial Transformation Training Centre in Additive Biomanufacturing (IC160100026). http://www.additivebiomanufacturing.org. Sandia National Laboratories is a multi-mission laboratory managed and operated by National Technology and Engineering Solutions of Sandia, LLC., a wholly owned subsidiary of Honeywell International, Inc., for the U.S. Department of Energy's National Nuclear Security Administration under contract DE-NA-0003525. The views expressed in the article do not necessarily represent the views of the U.S. Department of Energy or the United States Government. John Jakeman's work was supported by the U.S. Department of Energy, Office of Science, Office of Advanced Scientific Computing Research, Scientific Discovery through Advanced Computing (SciDAC) program.

Appendix A. Statistical Analysis Results

Histogram and best-fit distributions for every distinct combination of load case, strut build inclination angle and node classification. The following are abbreviations of each combination: Cell Wall (CW); Internal Cell Edge – load applied to 90° strut (ICE - 90°); Internal Cell Edge – load applied to 45° strut (ICE - 45°); External Lattice Face – load applied to 90° strut (ELF - 90°); External Lattice Face – load applied to external 45° strut (ELF – 45° (P)); External Lattice Face – load applied to internal 45° strut (ELF – 45° (I)); External Lattice Corner – load applied to 90° strut (ELC - 90°); External Lattice Corner – load applied to 45° strut (ELC - 45°).

CW – Load Case 1	CW – Load Case 2	CW – Load Case 3
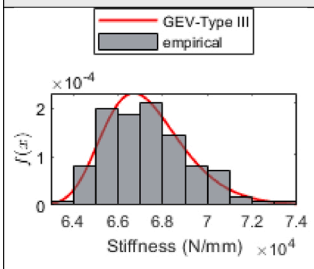	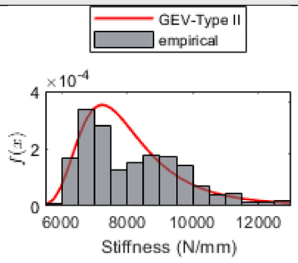	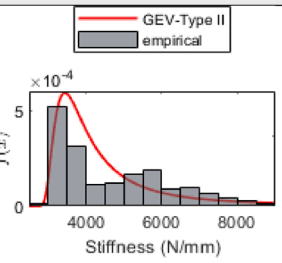
ICE 90° - Load Case 1	**ICE 90° - Load Case 2**	**ICE 90° - Load Case 3**
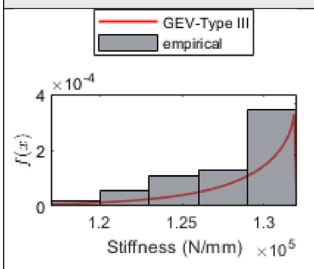	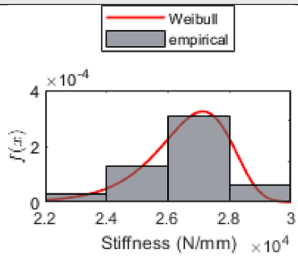	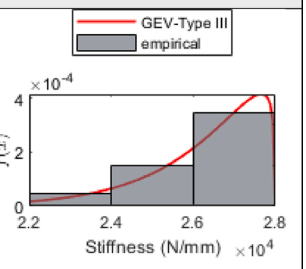
ICE 45° - Load Case 1	**ICE 45° - Load Case 2**	**ICE 45° - Load Case 3**
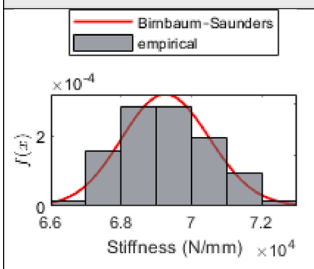	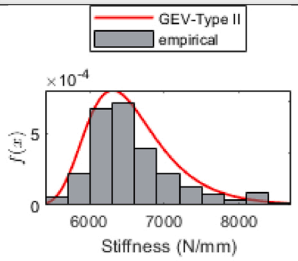	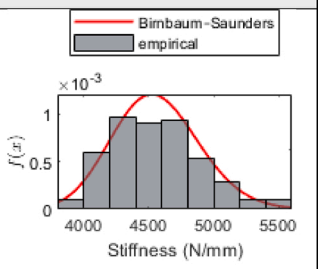
ELF 90° - Load Case 1	**ELF 90° - Load Case 2**	**ELF 90° - Load Case 3**
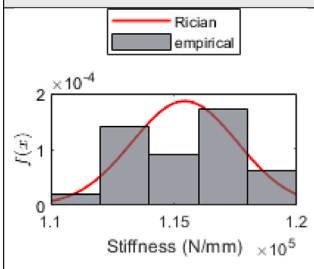	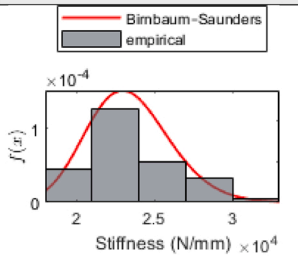	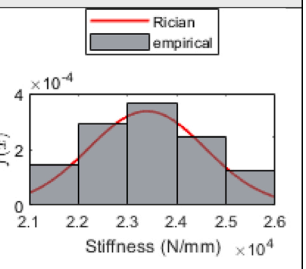
ELF 45° (P) - Load Case 1	**ELF 45° (P) - Load Case 2**	**ELF 45° (P) - Load Case 3**

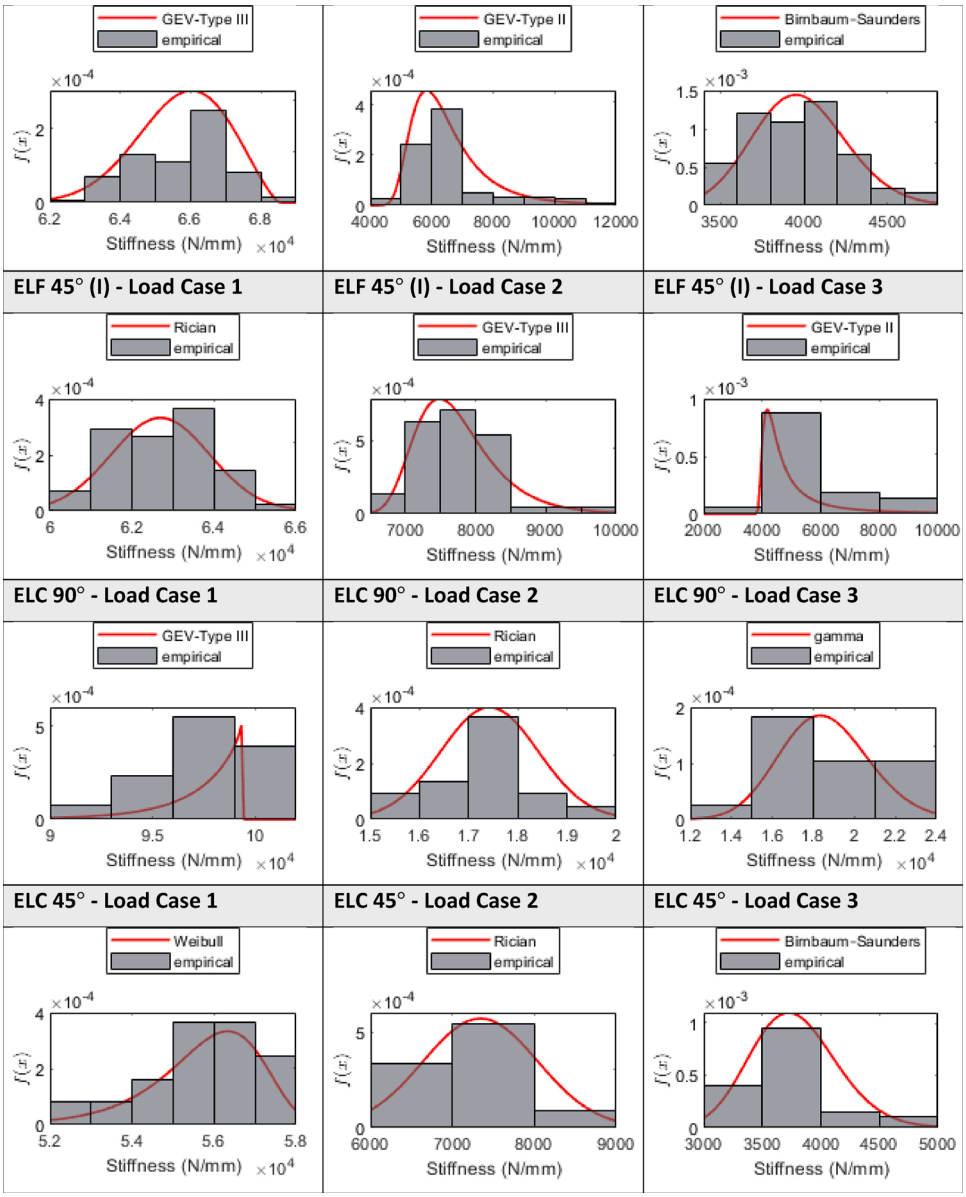

Appendix B. Empirical, best-fit and kernel density estimate cumulative density functions and cumulative denisty functions estimates

The empirical cumulative distribution functions and confidence intervals for every distinct combination of load case, strut build inclination angle and node classification. The cumulative distribution function from the kernel density estimation and best-fit probability distributions are also displayed. The best-fit cumulative distribution function can be referenced from Appendix A or Table 6. The following are abbreviations of each combination: Cell Wall (CW); Internal Cell Edge – load applied to 90° strut (ICE - 90°); Internal Cell Edge – load applied to 45° strut (ICE - 45°); External Lattice Face – load applied to 90° strut (ELF - 90°); External Lattice Face – load applied to external 45° strut (ELF – 45° (P)); External Lattice Face – load applied to internal 45° strut (ELF – 45° (I)); External Lattice Corner – load applied to 90° strut (ELC - 90°); External Lattice Corner – load applied to 45° strut (ELC - 45°).

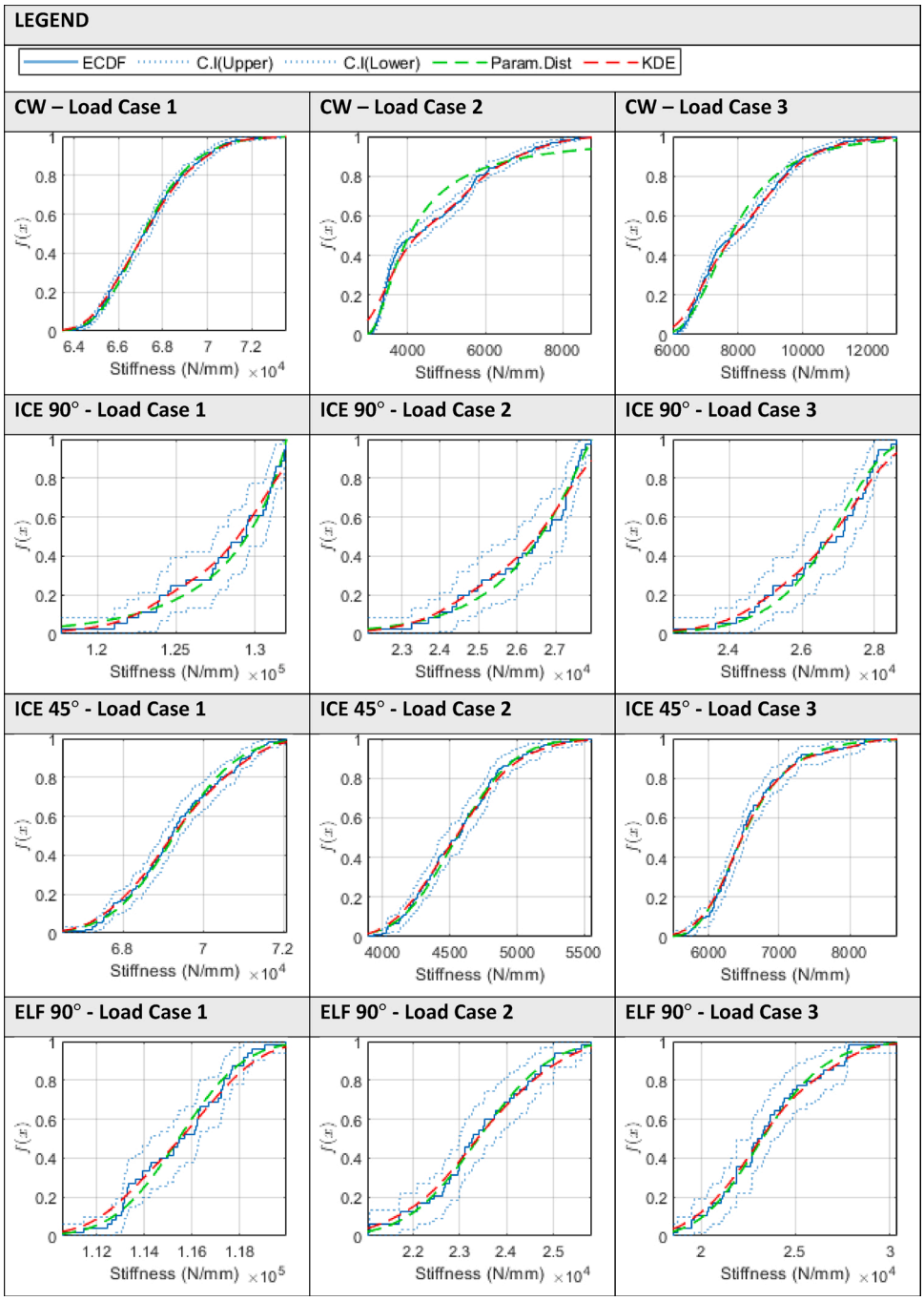
LEGEND
ECDF
C.I(Upper)
C.I(Lower)
Param.Dist
KDE
CW – Load Case 1
CW – Load Case 2
CW – Load Case 3
ICE 90° - Load Case 1
ICE 90° - Load Case 2
ICE 90° - Load Case 3
ICE 45° - Load Case 1
ICE 45° - Load Case 2
ICE 45° - Load Case 3
ELF 90° - Load Case 1
ELF 90° - Load Case 2
ELF 90° - Load Case 3
f(x)
Stiffness (N/mm)

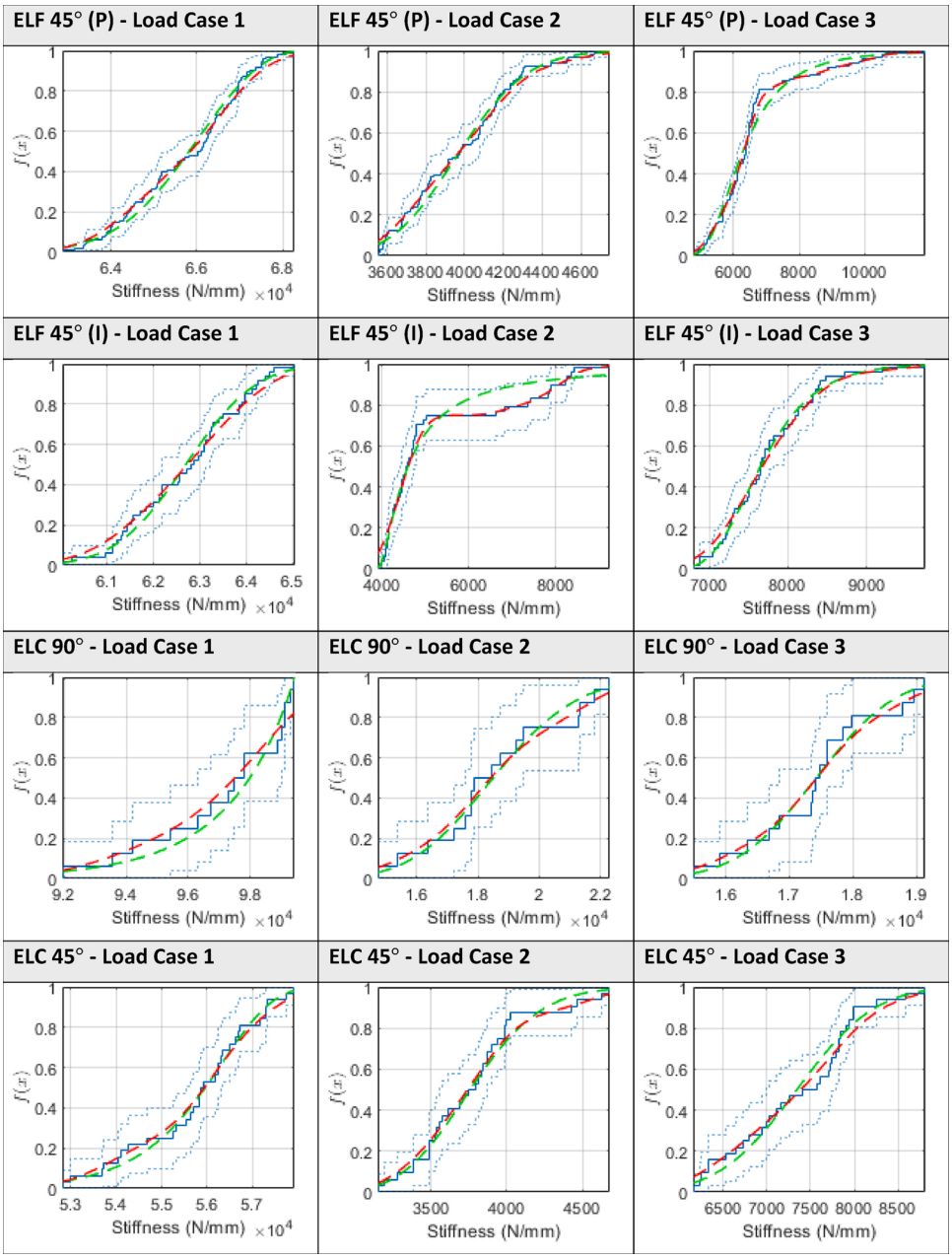

References

[1] L.J. Gibson, M.F. Ashby, Cellular Solids: Structure and Properties, Cambridge university Press, 1999.

[2] T. Maconachie, et al., SLM lattice structures: properties, performance, applications and challenges, Mater. Des. (2019) 108137.

[3] P. Terriault, V. Brailovski, Modeling and simulation of large, conformal, porosity-graded and lightweight lattice structures made by additive manufacturing, Finite Elem. Anal. Des. 138 (2018) 1–11.

[4] K.J. Maloney, et al., Multifunctional heat exchangers derived from three-dimensional micro-lattice structures, Int. J. Heat Mass Transf. 55 (9–10) (2012) 2486–2493.

[5] K.N. Son, et al., Design of multifunctional lattice-frame materials for compact heat exchangers, Int. J. Heat Mass Transf. 115 (2017) 619–629.

[6] G. Imbalzano, et al., A numerical study of auxetic composite panels under blast loadings, Compos. Struct. 135 (2016) 339–352.

[7] G. Imbalzano, et al., Three-dimensional modelling of auxetic sandwich panels for localised impact resistance, J. Sandw. Struct. Mater. 19 (3) (2017) 291–316.

[8] P. Tran, C. Peng, Triply periodic minimal surfaces sandwich structures subjected to shock impact, J. Sandw. Struct. Mater. (2020), p. 1099636220905551.

[9] M. Mohseni, et al., Additive biomanufacturing of scaffolds for breast reconstruction, Addit. Manuf. 30 (2019) 100845.

[10] Y. Tang, et al., Lattice structure design and optimization with additive manufacturing constraints, IEEE Trans. Autom. Sci. Eng. 15 (4) (2017) 1546–1562.

[11] A.A. Zadpoor, Additively manufactured porous metallic biomaterials, J. Mater. Chem. B 7 (26) (2019) 4088–4117.

[12] G.E. Ryan, A.S. Pandit, D.P. Apatsidis, Porous titanium scaffolds fabricated using a rapid prototyping and powder metallurgy technique, Biomaterials 29 (27) (2008) 3625–3635.

[13] J. Van der Stok, et al., Selective laser melting-produced porous titanium scaffolds regenerate bone in critical size cortical bone defects, J. Orthop. Res. 31 (5) (2013) 792–799.

[14] X. Tan, et al., Metallic powder-bed based 3D printing of cellular scaffolds for orthopaedic implants: a state-of-the-art review on manufacturing, topological design, mechanical properties and biocompatibility, Mater. Sci. Eng. C 76 (2017) 1328–1343.

[15] A. Alghamdi, et al., Experimental and numerical assessment of surface roughness for Ti6Al4V lattice elements in selective laser melting, Int. J. Adv. Manuf. Technol. 105 (1) (2019) 1275–1293.
[16] C. Calladine, Buckminster Fuller's "tensegrity" structures and Clerk Maxwell's rules for the construction of stiff frames, Int. J. Solids Struct. 14 (2) (1978) 161–172.
[17] V. Deshpande, M. Ashby, N. Fleck, Foam topology: bending versus stretching dominated architectures, Acta Mater. 49 (6) (2001) 1035–1040.
[18] J.C. Maxwell, L. on the calculation of the equilibrium and stiffness of frames, Lond. Edinb. Dub. Philos. Mag. J. Sci. 27 (182) (1864) 294–299.
[19] S.L. Sing, F.E. Wiria, W.Y. Yeong, Selective laser melting of lattice structures: a statistical approach to manufacturability and mechanical behavior, Robot. Comput. Manuf. 49 (2018) 170–180.
[20] Y. Xu, et al., Mechanical properties tailoring of topology optimized and selective laser melting fabricated Ti6Al4V lattice structure, J. Mech. Behav. Biomed. Mater. 99 (2019) 225–239.
[21] V. Weißmann, et al., Comparison of single Ti6Al4V struts made using selective laser melting and electron beam melting subject to part orientation, Metals 7 (3) (2017) 91.
[22] M. Mazur, et al., Deformation and failure behaviour of Ti-6Al-4V lattice structures manufactured by selective laser melting (SLM), Int. J. Adv. Manuf. Technol. 84 (5–8) (2016) 1391–1411.
[23] I. Echeta, et al., Review of defects in lattice structures manufactured by powder bed fusion, Int. J. Adv. Manuf. Technol. (2019) 1–20.
[24] M. Leary, et al., Inconel 625 lattice structures manufactured by selective laser melting (SLM): mechanical properties, deformation and failure modes, Mater. Des. 157 (2018) 179–199.
[25] M. Leary, et al., Selective laser melting (SLM) of AlSi12Mg lattice structures, Mater. Des. 98 (2016) 344–357.
[26] E. Hernández-Nava, et al., The effect of defects on the mechanical response of Ti-6Al-4V cubic lattice structures fabricated by electron beam melting, Acta Mater. 108 (2016) 279–292.
[27] M. Dallago, et al., Fatigue and biological properties of Ti-6Al-4V ELI cellular structures with variously arranged cubic cells made by selective laser melting, J. Mech. Behav. Biomed. Mater. 78 (2018) 381–394.
[28] C. Peng, et al., Mechanical performance and fatigue life prediction of lattice structures: parametric computational approach, Compos. Struct. 235 (2020).
[29] L. Yang, et al., An investigation into the effect of gradients on the manufacturing fidelity of triply periodic minimal surface structures with graded density fabricated by selective laser melting, J. Mater. Process. Technol. 275 (2020) 116367.
[30] A. Du Plessis, et al., X-ray microcomputed tomography in additive manufacturing: a review of the current technology and applications, 3D Print. Addit. Manuf. 5 (3) (2018) 227–247.
[31] A. du Plessis, et al., Beautiful and functional: a review of biomimetic design in additive manufacturing, Addit. Manuf. 27 (2019) 408–427.
[32] C. Peng, P. Tran, Bioinspired functionally graded gyroid sandwich panel subjected to impulsive loadings, Compos. Part B Eng. 188 (2020).
[33] A.C. Kak, M. Slaney, G. Wang, Principles of computerized tomographic imaging, Med. Phys. 29 (1) (2002), 107-107.
[34] E. Maire, P.J. Withers, Quantitative X-ray tomography, Int. Mater. Rev. 59 (1) (2014) 1–43.
[35] L. De Chiffre, et al., Industrial applications of computed tomography, CIRP Ann. Manuf. Technol. 63 (2) (2014) 655–677.
[36] A. du Plessis, M. Tshibalanganda, S. le Roux, Not all scans are equal: X-ray tomography image quality evaluation, Mater. Today Commun. 22 (2020) 100792.
[37] E. ASTM, 1570-11-Standard Practice for Computed Tomographic (CT) Examination, ASTM International, United States, 2011.
[38] A. Du Plessis, et al., Laboratory X-ray tomography for metal additive manufacturing: round robin test, Addit. Manuf. 30 (2019) 100837.
[39] Z. Xiao, et al., Evaluation of topology-optimized lattice structures manufactured via selective laser melting, Mater. Des. 143 (2018) 27–37.
[40] A. du Plessis, I. Yadroitsava, I. Yadroitsev, Ti6Al4V lightweight lattice structures manufactured by laser powder bed fusion for load-bearing applications, Opt. Laser Technol. 108 (2018) 521–528.
[41] Y. Amani, et al., Compression behavior of lattice structures produced by selective laser melting: X-ray tomography based experimental and finite element approaches, Acta Mater. 159 (2018) 395–407.
[42] V. Tvergaard, On localization in ductile materials containing spherical voids, Int. J. Fract. 18 (4) (1982) 237–252.
[43] C. Petit, et al., Two-scale study of the fracture of an aluminum foam by X-ray tomography and finite element modeling, Mater. Des. 120 (2017) 117–127.
[44] M. Smith, Z. Guan, W. Cantwell, Finite element modelling of the compressive response of lattice structures manufactured using the selective laser melting technique, Int. J. Mech. Sci. 67 (2013) 28–41.
[45] M.H. Luxner, J. Stampfl, H.E. Pettermann, Finite element modeling concepts and linear analyses of 3D regular open cell structures, J. Mater. Sci. 40 (22) (2005) 5859–5866.
[46] A.C. Jones, R.K. Wilcox, Assessment of factors influencing finite element vertebral model predictions, J. Biomech. Eng. 129 (6) (2007) 898–903.
[47] L.E. Schwer, Guide for Verification and Validation in Computational Solid Mechanics, 2009.
[48] D. Shidid, et al., Just-in-time design and additive manufacture of patient-specific medical implants, Phys. Procedia 83 (2016) 4–14.
[49] S.R. de Galarreta, J.R. Jeffers, S. Ghouse, A validated finite element analysis procedure for porous structures, Mater. Des. 189 (2020) 108546.
[50] M. Suard, et al., Towards stiffness prediction of cellular structures made by electron beam melting (EBM), Powder Metall. 57 (3) (2014) 190–195.
[51] M. Suard, et al., Mechanical equivalent diameter of single struts for the stiffness prediction of lattice structures produced by Electron Beam Melting, Addit. Manuf. 8 (2015) 124–131.
[52] H. Lei, et al., Evaluation of compressive properties of SLM-fabricated multi-layer lattice structures by experimental test and μ-CT-based finite element analysis, Mater. Des. 169 (2019) 107685.
[53] A. Alghamdi, et al., Effect of polygon order on additively manufactured lattice structures: a method for defining the threshold resolution for lattice geometry, Int. J. Adv. Manuf. Technol. 105 (5–6) (2019) 2501–2511.
[54] R. Mines, Additive manufacturing processes and materials for metallic microlattice structures using selective laser melting, electron beam melting and binder jetting. Metallic Microlattice Structures, Springer, 2019, pp. 17–31.
[55] G. Labeas, M. Sunaric, Investigation on the static response and failure process of metallic open lattice cellular structures, Strain 46 (2) (2010) 195–204.
[56] V. Crupi, et al., Static behavior of lattice structures produced via direct metal laser sintering technology, Mater. Des. 135 (2017) 246–256.
[57] B. Lozanovski, et al., A Monte Carlo simulation-based approach to realistic modelling of additively manufactured lattice structures, Addit. Manuf. 32 (2020) 101092.
[58] L. Liu, et al., Elastic and failure response of imperfect three-dimensional metallic lattices: the role of geometric defects induced by Selective Laser Melting, J. Mech. Phys. Solids 107 (2017) 160–184.
[59] K. Refai, et al., Determination of the effective elastic properties of titanium lattice structures, Mech. Adv. Mater. Struct. (2019) 1–14.
[60] M. Dallago, et al., On the effect of geometrical imperfections and defects on the fatigue strength of cellular lattice structures additively manufactured via Selective Laser Melting, Int. J. Fatigue 124 (2019) 348–360.
[61] M. McMillan, et al., Programmatic lattice generation for additive manufacture. DesTech2015, 2015, pp. 178–184. Geelong, Australia.
[62] J. Kittler, J. Illingworth, J. Föglein, Threshold selection based on a simple image statistic, Comput. Vis. Graph. Image Process. 30 (2) (1985) 125–147.
[63] B. Lozanovski, et al., Image-based geometrical characterisation of nodes in 3D printed lattice structures, 3D Print. Addit. Manuf. (2020) (In Press).
[64] A.W. Bowman, A. Azzalini, Applied Smoothing Techniques for Data Analysis: the Kernel Approach with S-Plus Illustrations, Vol. 18, OUP Oxford, 1997.
[65] L. Yang, et al., Compression–compression fatigue behaviour of gyroid-type triply periodic minimal surface porous structures fabricated by selective laser melting, Acta Mater. 181 (2019) 49–66.